

EXTRATROPICAL LAPSE RATES IN VERY HOT CLIMATES

A Thesis

by

RYAN ALEXANDER ZAMORA

Submitted to the Office of Graduate Studies of
Texas A&M University
in partial fulfillment of the requirements for the degree of

MASTER OF SCIENCE

Chair of Committee,	Robert Korty
Committee Members,	Courtney Schumacher
	Deborah Thomas
Head of Department,	Ping Yang

August 2013

Major Subject: Atmospheric Sciences

Copyright 2013 Ryan Alexander Zamora

ABSTRACT

The interplay between convective processes and the stabilizing effects of large-scale systems remains debated, especially for warmer climates. We study sets of simulations of past and present climates in which carbon dioxide (CO_2) concentrations vary over a wide range: from pre-industrial era levels of 280 ppm to an exceedingly high value of 8960 ppm. This allows us to assess the importance of convective processes relative to middle latitude thermal stratification and changes to the general circulation in progressively warmer climate states.

As a tool to assess the stability of the atmosphere, we calculate a thermodynamic variable called saturation potential vorticity (P^*), which has the property of being identically zero wherever lapse rates are neutral with respect to moist convection, and large where lapse rates are stable. Using P^* allows us to examine convective motions arising from both gravitational accelerations as well as symmetric instabilities.

We assess the ability of current models (of varying spectral resolutions) in resolving conditions unstable to slantwise convection. We show that the coarse resolution reanalysis data captures instances of observed slantwise convection. Our results show examples of vertically stable lapse rates, while being conditionally unstable along slanted angular momentum surfaces. This suggests the need for model parameterizations of convection to include instabilities arising from symmetric displacements.

Tropical regions are neutral with respect to moist convection while higher latitudes most often have stable lapse rates, especially during the winter months. In the warmer climate simulations, the frequency of convectively neutral air masses increases in both middle latitude and polar regions, especially during the summer months. These simulations also show expansion of the Hadley cell and shifting of middle latitude storm tracks. Using Maximum Potential Intensity (*MPI*) as a tool to assess the upper bound of hurricane strength, we show sustainment of intense tropical cyclones in regions they cannot in our present climate.

DEDICATION

To My Brother

ACKNOWLEDGEMENTS

I would like to acknowledge my advisor, Dr. Robert Korty, whose guidance through this research and thesis cannot be understated. Thank you for showing trust in my abilities, and for always treating me as a colleague. I look forward to continued work with you. In addition, I would like to thank my committee members, Dr. Courtney Schumacher and Dr. Debbie Thomas, for their time, support, and patience.

I thank my officemates, both past and present, for their help and always making the workdays enjoyable. I also would like to extend my thanks to the Department of Atmospheric Sciences faculty and staff for always having open doors to any thoughts, questions, and concerns.

A special thank you goes to my friends and family for all their prayers, unending support, making me laugh, and gifting me an occasional cupcake. I would especially like to thank Misti for her help on a day-to-day basis. Thank you for always pulling me forward and keeping my head on straight.

Lastly, I would like to specifically thank my parents. No one has ever believed in me as much they have, and I wouldn't be where I am today without them.

TABLE OF CONTENTS

	Page
ABSTRACT	ii
DEDICATION	iv
ACKNOWLEDGEMENTS	v
TABLE OF CONTENTS	vi
1. INTRODUCTION AND BACKGROUND	1
2. SATURATION POTENTIAL VORTICITY	7
3. REPRESENTATIONS OF SLANTWISE CONVECTIVE NEUTRALITY IN MODELS OF DIFFERENT RESOLUTION	11
3.1 Case Study: 16 November 1983	12
3.2 Case Study: 26 January 1986	14
3.3 Case Study: 10 February 1986	15
4. CCSM MODEL INFORMATION AND METHODOLOGY	16
4.1 Present Day Climate Scenarios	17
4.2 Pre-Industrial Climate Scenarios	17
4.3 Eocene Climate Scenarios	18
4.4 Constant Ocean Eocene Climate Scenarios	19
5. PRESENT CLIMATE	21
6. DIAGNOSING LAPSE RATES IN WARMER CLIMATES	24
6.1 P^* Variability in a Warming Climate	24
6.2 Relative Magnitudes of Horizontal Components	27
6.3 Temporal Resolution Dependence of P^*	28
7. HADLEY CELL CIRCULATION AND TRANSIENT EDDIES	30
8. SOUNDINGS AND MIDLATITUDE STORM TRACKS	33
8.1 Implications of a Warming Climate	40

	Page
9. EOCENE AND PRE-INDUSTRIAL SCENARIO DIFFERENCES	42
10. CONCLUSIONS	45
REFERENCES	48
APPENDIX A	53
APPENDIX B	55
APPENDIX C	56

1. INTRODUCTION AND BACKGROUND

Extratropical storms redistribute heat from the tropics to high latitudes, pushing warm tropical air poleward on their eastern sides and bringing cold polar air equatorward to their west. Analyses of vertical transport of heat fluxes in baroclinic waves show that they also transport heat vertically, stabilizing atmospheric lapse rates (e.g., *Held*, 1982; *Gutowski et al.*, 1992). While tropical lapse rates are nearly neutral with respect to moist convection (*Xu and Emanuel*, 1989), lapse rates at higher latitudes are typically characterized by relatively large stability with respect to moist convection (e.g., *Stone and Carlson*, 1979). As convection occurs within baroclinic eddies, the roles that convective processes and dynamics play in establishing the observed static stability of the extratropical atmosphere is complex and challenging to distinguish (e.g., *Juckes*, 2000).

In the tropics, where horizontal temperature gradients are weak, convective processes act in concert with radiation and large-scale circulations to establish a basic state temperature structure. Emanuel et al. (1994) argued that convective processes directly establish the vertical temperature profile, which is consistent with observations by Betts (1982) that lapse rates in the tropics are commonly neutral with respect to moist convection. Illustrations of this are available in plots of saturation entropy s^* or the saturation equivalent potential temperature θ_e^* , which are thermodynamic state variables (either can be determined by combining any other two state variables, such as temperature and pressure) throughout the tropics (e.g., *Korty and Schneider*, 2007). As these quantities are constant along moist adiabatic profiles, lapse rates are neutral with

respect to moist convection where s^* (and therefore θ_e^*) is constant with respect to height. This state is common throughout the tropics (*Xu and Emanuel, 1989*).

Although convection occurs outside of the tropics, much of the work on extratropical lapse rates has concentrated on the dominating role of dry dynamics. Stone (1978) examined the idea that baroclinic eddies play a defining role in regulating the strength of the meridional temperature gradient and vertical lapse rate. Using the architecture of Phillip's (1954) two-layer model, he showed that atmospheric stability could be predicted by examining the relationship between vertical wind shear (or, by the thermal wind relationship, the meridional temperature gradient) and a critical shear value; when shear is stronger than this threshold, the two-layer model is unstable to baroclinic instabilities; when weaker, it is stable. Stone (1978) proposed that once the temperature gradient or wind shear was perturbed beyond the critical point, baroclinic processes would always adjust the atmosphere to a state neutral with respect to baroclinic instability, leading to a cyclical process where waves grow and subsequently decay. This process is called baroclinic adjustment.

The basic tenet of this argument is that because the latitudinal distribution of temperature produced by radiative-convective equilibrium is unstable to baroclinic waves, dynamic instabilities grow from infinitesimal perturbations, which then in turn relax the supercritical temperature gradient to a neutral state with respect to their existence. Meridional temperature gradients naturally reach a supercritical value due to differential diabatic heating, allowing conditions to become favorable for growth of long, deep waves. As these waves mature, they produce an eddy flux that reduces the

strength of the gradient to subcritical values. After this transport of heat has stalled, waves begin to stabilize and decay, resulting in a weakening eddy flux. Finally, the atmosphere again undergoes diabatic processes, which generate a temperature gradient again exceeding the critical value. This process of baroclinic adjustment expresses the relationship between the meridional temperature gradient and the effects of transient eddies without the necessity of actual eddy kinetic energy calculations; this allows the effects of eddies on the large-scale thermal structure to be parameterized in simpler energy balance models (e.g., *North, 1975; Stone, 1978*). Given the fundamental aspects of this type of interaction to extratropical dynamics, a central role for their importance in maintaining the vertical stability of the extratropical troposphere has been advocated by authors for several decades (e.g., *Stone, 1978; Lindzen et al., 1980; Held, 1982; Gutowski, 1985; Gutowski et al., 1989; Lindzen, 1993; Stone and Nemet, 1996; Schneider, 2007*).

Observed lapse rates in the extratropics are about $6.5\text{ }^{\circ}\text{C km}^{-1}$ (*Brunt, 1933*), which is more stable than moist adiabatic profiles, but there are significant seasonal and latitudinal deviations (*Stone and Carlson, 1979*). These variations mainly originate from the varying relevance of moist convection and baroclinic eddies in establishing local lapse rates (e.g. eddies are most effective at stabilizing the atmosphere in winter in middle and high latitudes). *Stone and Carlson (1979)* concluded that in order to examine the interaction between the vertical and meridional temperature structure, the use of a radiative-convective equilibrium model with two critical lapse rates had to be

implemented: the lapse rate would then be constrained by the moist adiabatic lapse rate and the critical value for baroclinic adjustment.

Yet more recently, Barry et al. (2000) showed that the baroclinic adjustment process does not accurately capture what happens in nature. He posited that the time it takes for the atmosphere to relax to radiative equilibrium and the timescale on which baroclinic eddies act on the flow were far too close to be distinguished. In order for a truly neutral baroclinic state to be observed, the baroclinic adjustment timescale must be much faster than what was originally proposed. Jukes (2000) has argued that moist convection in the warm sector of baroclinic waves acts in concert with the eddy itself to determine the ultimate thermal stratification.

Moreover, the effects of convection on lapse rates can be difficult to see through conventional analyses. While convective processes that occur along the effective gravitational vector (which incorporates the centrifugal force, and is directed normal to the level surface) neutralize vertical soundings, convective motions that occur along slanted angular momentum surfaces do not. Rotating systems experience centrifugal accelerations, and fluids respond to unstable distributions of angular momentum along this vector in the same way as they do to unstable distributions of mass along the effective gravitational vector (cf. Chapter 12, *Emanuel*, 1994). The response to these inertial accelerations is called symmetric instabilities (*Bennetts and Hoskins*, 1979; *Emanuel*, 1983a), and convection may be driven by it, conventional upright accelerations along the gravitational vector, or a combination of the two. These “slantwise” convective motions occur along surfaces of constant angular momentum,

which may be strongly tilted from the vertical in strongly rotating systems. Emanuel (1983b, 1988) presented several case studies of regions near frontal boundaries in which slantwise convection had occurred. In these cases, conventional analyses of vertical soundings at a single station showed lapse rates stable to moist convection, emphasizing the need for tools to diagnose instances of convection that occur along slanted paths through the atmosphere.

These complexities highlight the importance of diagnosing how frequently lapse rates neutral to moist convective processes occur. Korty and Schneider (2007) documented that lapse rates nearly neutral to moist convection along surfaces of constant angular momentum are common features of the extratropics over continents during summer and in ocean storm tracks throughout the year. One of the principal goals of this thesis is to ascertain how this climatology may vary with climate, and we utilize simulations of increasingly hot atmospheres to diagnose the response. Slantwise convective motions are not generally parameterized in large-scale models, and this leads to a question of whether or not coarse resolution grids are capable of simulating cases that could be neutralized by these processes.

We first illustrate that coarse resolution reanalysis products capture many of the examples of slantwise convective neutrality documented in case studies and field campaigns (Section 3). We then proceed to analyze how the frequencies of these states vary with climate in simulations using NCAR's Community Climate System Model (Section 6). Afterwards, we examine the sensitivity of the general circulation to different climate states (Section 7) and the implications this has on midlatitude storm tracks

(Section 8). Finally, we provide a brief assessment of the effects paleogeography may have on modifying these findings (Section 9).

2. SATURATION POTENTIAL VORTICITY

In our present climate, lapse rates are neutral with respect to moist convection in the tropics (*Xu and Emanuel, 1989*), but are stable poleward. In the midlatitudes (30° - 60°), large-scale eddies stabilize the troposphere, but convection still occurs in the region. This is especially true over continents in summer and in winter storm tracks over oceans (*Korty and Schneider, 2007*). As such, we examine the evolution of the role convection plays in a warming climate.

In our diagnosis of the atmospheric thermal structure, we consider convective displacements that arise from both gravitational and inertial accelerations. While angular momentum (M) surfaces are commonly oriented parallel to the effective gravity vector, in large rotating systems (e.g. midlatitude cyclones) they may tilt with height. Convection flowing along these tilted, curving surfaces is referred to as slantwise convection, and its inclusion is important for our study of stability in the midlatitudes. A defining feature of moist adiabatic lapse rates is that the saturation equivalent potential temperature θ_e^* , or its logarithm saturation entropy s^* , is constant. These quantities are thermodynamic state variables, which mean they belong to a family of variables sharing the property that knowledge of any two can exclusively determine any other. (Examples of these include temperature, pressure, density, entropy, saturation mixing ratio,

saturation specific humidity, and saturation entropy) The saturation entropy is defined approximately¹ (*Emanuel, 2007*) as:

$$s^* = c_p \ln\left(\frac{T}{T_0}\right) - R_d \ln\left(\frac{p}{p_0}\right) + \frac{L_v q^*}{T} \quad (1)$$

In Equation 1, T_0 and p_0 are reference temperatures and pressure, respectively, c_p is the heat capacity at constant pressure, L_v is the latent heat of vaporization (itself a function of temperature), and q^* is the saturation specific humidity, which can also be determined from temperature and pressure. Thus s^* (and θ_e^* , to which it is related logarithmically), is determined solely by a parcel's temperature T and pressure p .

Along moist adiabats, s^* is constant. This is straightforward to assess vertically, as the value of θ_e^* will be constant on a convectively neutral sounding. But assessing neutrality along an angular momentum surface that deflects from the vertical direction requires an alternate approach. Emanuel (2008) showed that one of the moist variants of Ertel's potential vorticity can be utilized to assess convective neutrality along angular momentum surfaces, which are often upright, but can deviate when centrifugal accelerations become non-negligible.

Because surfaces of angular momentum are oriented parallel to the absolute vorticity vector (cf. *Frisius, 2005; Korty and Schneider, 2007*), we can assess convective stability along any angular momentum surface by assessing how θ_e^* changes along the vorticity vector. Saturation potential vorticity P^* is modified from Ertel's potential

¹ In our analysis, we calculate saturation equivalent potential temperature exactly following the definition given on page 120 of Emanuel (1994). Calculating this variable precisely is not trivial, and we review the procedure more thoroughly in Appendix A.

vorticity P by replacing potential temperature (θ) with saturation equivalent potential temperature (θ_e^*). Thus, it is identically zero wherever lapse rates are neutral with respect to moist convection along this vector. It is defined as

$$P^* = \text{sign}(f) \alpha \vec{\xi}_{abs} \cdot \nabla \theta_e^* \quad (2)$$

where α is the specific volume and $\vec{\xi}_{abs}$ is the absolute vorticity vector; the $\text{sgn}(f)$ term is a multiplicative factor of -1 in the Southern Hemisphere, and +1 in the Northern Hemisphere to enforce the parity of P^* to have the same meaning globally. Although P^* is not conserved in unsaturated air, it is ideally suited to diagnose moist adiabatic lapse rates that arise from both upright and slantwise convection. P^* will be approximately zero wherever lapse rates are nearly moist adiabatic along angular momentum surfaces, positive in stably stratified fluids, and negative when lapse rates are larger (e.g. the dry adiabatic lapse rates common in deserts and boundary layers).

Having the inherent quality of differentiating between stable and convectively adjusted air masses makes P^* a powerful tool for diagnosing lapse rates. While straightforward in nature, its underlying function is worth exploring in further detail. Slantwise convective neutrality occurs when M -surfaces and lines of constant θ_e^* are parallel (i.e. in the direction of the vorticity vector). Tracking how θ_e^* changes along a parcel of air displaced along an M -surface will determine the resultant air mass stability.

Figure 1 shows a basic schematic (adapted from *Emanuel, 1983*) of how this relationship works. The square located at the surface represents a theoretical parcel of air, while isolines of M and θ_e^* are indicated by a dashed and solid line, respectively. Both values increase in the positive x and z-directions. If θ_e^* increases (decreases)

upward along a slanted M -surface, a parcel will be stable (unstable) to slantwise moist convection. A parcel displaced to the position denoted by “A” will undergo a decrease in θ_e^* and be stable ($P^* > 0$). A parcel displaced to position “B” (intersection of isolines of M and θ_e^*) will be neutral to moist convection ($P^* = 0$). Displacing a parcel to position “C” will undergo a decrease in θ_e^* and be convectively unstable ($P^* < 0$). This simple relation (an intrinsic property of P^*) gives us a method to diagnose stability.

3. REPRESENTATIONS OF SLANTWISE CONVECTIVE NEUTRALITY IN MODELS OF DIFFERENT RESOLUTION

Before we proceed to analyze how the climatology of extratropical lapse rates varies in simulations over a wide range of climate states, we first address the issue of whether coarse resolution models are capable of resolving conditions necessary for slantwise convective motions to occur. Korty and Schneider (2007) examined the climatology of slantwise convective neutrality in 35 years of daily-averaged reanalysis data contained in the NCEP/NCAR reanalysis, which has horizontal grid spacing of 2.5° in latitude and longitude. While they found that datasets at this resolution contain many additional cases of convective neutrality along slanted paths (in addition to the more conventional upright-convective neutrality), it remains unclear how (both spatially and temporally) higher resolution datasets might differ. Korty and Schneider (2007) compared their findings over North America with identical calculations performed on the higher resolution North American Regional Reanalysis (NARR), and found similar results over land, but differing frequencies over data sparse oceans.

Emanuel (1983b, 1988) presented some of the earliest case studies of slantwise convective neutrality using observations from field campaigns (e.g., New England Winter Storms Experiment (NEWS), Genesis of Atlantic Lows Experiment (GALE), and Canadian Atlantic Storms Program) and by constructing cross sections using data from neighboring rawinsondes. To see how reanalysis sets of different resolutions handle observed cases of slantwise convective neutrality, we revisit three cases Emanuel (1988) studied using three separate reanalysis products: Modern Era Retrospective-analysis for

Research and Application's inst3_3d_asm_Cp model (henceforth MERRA), Earth Systems Research Laboratories CIRES 20th Century Reanalysis 2 (henceforth 20CR), and NCEP/NCAR Reanalysis 2 Project (henceforth NCEP). These particular models were chosen for their varying degrees of spatial resolution: 1.25° x 1.25° with 42 pressure levels (MERRA), 2° x 2° with 24 pressure levels (20CR), and ~2.5° x 2.5° with 17 pressure levels (NCEP).

We examine three observational case studies of slantwise convection: a New England coastal front on 16 November 1983, and sectors near a warm-frontal boundary in the eastern United States on 26 January 1986, and another on 10 February 1986. The purpose of these studies was to see whether slantwise convection actually occurs. The approach used was two-fold: (1) neighboring rawinsondes were combined to create a vertical cross-section of θ_e^* and M , and (2) an instrumented aircraft flew along an M -surface so that its alignment with surfaces of θ_e^* could be examined later. The specific methodology used is detailed in Emanuel (1988). Our goal here is to examine cross sections of P^* in these situations, which were observed to be neutral to slantwise convection. Using datasets of varying spatial resolution provides insight to the ability of coarser models in reproducing slantwise convection.

3.1 Case Study: 16 November 1983

This study examined data from rawinsondes originating at 3 different locations: Caribou, Maine (CAR), Portland, Maine (PWM), and Chatham, Massachusetts (CHH). These sites are plotted in Figure 2a for 0000 UTC 16 November 1983 along with surface

analysis as calculated by the highest resolution dataset, MERRA. There is a high degree of agreement between the modeled atmospheric setup with the observed large-scale weather features from the case study. A low-pressure center is located to the southeast of the flight trajectory location (Brunswick, Maine). Warm air advection associated with a coastal warm front was occurring throughout the region. Results from Emanuel (1988) found slantwise convection at 600 – 300 hPa in between PWM and CHH. Figure 2b is a horizontal projection of P^* taken at the 500 hPa level showing the rawinsonde locations coincident with a convectively adjusted air masses ($P^* \leq 0$). The vertical cross section we examine (red line in Figure 2a) is taken along 70.625°W from 40°N to 45°N. Figure 2c depicts P^* along this line, showing that convective neutrality is in fact captured between 600 – 300 hPa. Interestingly, however, the vertical component of P^* ($-g[f + \xi]d\theta_e^*/dp$; shown in Figure 2d) is mostly stable ($P^* > 0$) through this region. This is an important finding that shows an example of lapse rates stable to upright convection, while being conditionally unstable to symmetric instabilities.

Figure 3 shows the same multi-panel plot as Figure 2, except using the coarser resolution NCEP reanalysis data. Similarly as with MERRA, the surface analysis is captured fairly well by the model. The 500 hPa plot of P^* (Figure 3b) suffers little from having less fine resolution, still depicting the desired region with values for $P^* < 0$. Likewise, the cross sections (Figures 3c & 3d; taken along 70°W) show a convectively neutral air mass that is stable (unstable) in the vertical (along slanted M -surfaces). This is an encouraging result that is replicated in the 2° x 2° resolution 20CR data as well (not shown).

3.2 Case Study: 26 January 1986

The 26 January 1986 case study examined rawinsondes throughout the eastern United States: Dayton, Ohio (DAY), Huntington, West Virginia (HTS), Greensboro, North Carolina (GSO), Fayetteville, North Carolina (FAY), and Wilmington, North Carolina (ILM). The locations of these sites are located on Figure 4a along with the MERRA modeled surface analysis at 1200 UTC. The large-scale features are captured and recreated by the model with a good degree of accuracy. The region of the flight trajectory taken is located in a region of a warm-frontal boundary associated with a near stationary front. Lapse rates along M -surfaces greater than or equal to the moist adiabatic lapse rate were found at the 4 most eastern sites through much of the free troposphere. Figure 4b shows all 5 sites coincide within regions where values of $P^* \leq 0$ at the 500 hPa level. Looking at P^* along 78.125°W from 33°N to 38°N (Figures 4c & 4d) yields lapse rates that are stable to upright convection, and convectively neutral to symmetric instabilities.

The lower resolution NCEP reanalysis data again shows its ability to reproduce slantwise convection. Figure 5b shows the sounding locations within regions of a convectively adjusted air mass at the 500 hPa level, while also showing convectively neutral lapse rates (Figures 5c & 5d) in the regions of slantwise convection determined in Emanuel (1988). All three models capture this feature, regardless of resolution.

3.3 Case Study: 10 February 1986

The final case examined by Emanuel (1988) occurred on 10 February 1986, again in the eastern United States: Petersburg, Virginia (PTB), Greenville, North Carolina (PGV), Fayetteville, North Carolina (FAY), Wilmington, North Carolina (ILM), Myrtle Beach, South Carolina (MYR), and Charleston, South Carolina (CHS). As in the previous cases, the surface analysis is well captured by all three models (Figures 6a & 7a). A warm front coupled with a low-pressure center to the southeast of the flight location (Fayetteville, North Carolina), brings warm air through the region and striated precipitation to its south. Moist adiabatic lapse rates along M -surfaces were found through a large portion of the sounding network throughout the free troposphere. Figures 6b & 7b confirm this, showing each location within 500 hPa values of $P^* < 0$. Figures 6c & 6d show P^* along 78.125°W from 33°N to 38°N , as calculated by MERRA. As with the previous studies, these plot show negative values of P^* through much of its coverage, concurrent with positive values of its vertical component. This result is reproduced by lower resolution data sets as well, as shown by the NCEP reanalysis (Figures 7c & 7d).

4. CCSM MODEL INFORMATION AND METHODOLOGY

Our primary objective is to understand how changes in the general circulation, in response to increased CO₂ concentrations, affect the thermal structure of the extratropics. To achieve this, we use output from NCAR's Community Atmospheric Model 3 at T42 spatial resolution ($\sim 2.5^\circ \times 2.5^\circ$, see *Caballero and Huber, (2010)* for further details) in which carbon dioxide levels vary over a wide range. The model is run using a prescribed ocean heat transport (OHT) and is coupled to a slab ocean, which simulates the overall effects of a dynamical ocean while being less computationally intensive. We examine 14 climate scenarios, including geographies for present day and during the early Eocene epoch and concentrations of CO₂ ranging from 280 – 8960 parts per million (ppm).

Each simulation is introduced a concentration of CO₂ and then run to equilibrium to provide a properly mixed atmosphere. The data is then averaged climatologically (i.e. over the wide range of available years) in order to represent conditions of a “typical” month. While we have examined simulations for various climates such as present day, pre-industrial, and the Eocene epoch, unless otherwise stated, results presented in this paper will be using present day conditions and geography.

Table 1 shows the averaged global sea surface temperature and number of available years for both monthly and 6-hourly data for each of these cases. The simulation names (further explained in the subsequent sections) are each appended with a number representative of the amount of doublings of CO₂ inherent in the model. The temporal resolution of the data varies on the calculation of the specific variable. High temporally sensitive calculations such as P^* are generated from data with a 6-hourly time

step, while other variables such as the transient eddy heat flux are created from monthly averaged data.

4.1 Present Day Climate Scenarios

The present day climate scenarios (prefixed “uhPD”) use a control CO₂ concentration of 355 ppm. This was the global averaged concentration in 1990, although presently that number is closer to 400 ppm (*Showstack*, 2013). These simulation names are appended with a number representative of the number of doublings of CO₂ inherent in the model. The model naming convention uses “uh” to refer to climate simulations that reach ultra hot temperatures, and “PD” to refer to the use of present day topography. As seen in Table 1, there are 3 cases for this scheme: the control, 3 doublings (2240 ppm), and 5 doublings (8960 ppm) of the pre-industrial value. This scheme uses a fixed solar constant of 1367 W/m² and includes aerosol forcings. We believe this scheme is most representative of our current climate, and as such data provided in this paper will derive from it.

4.2 Pre-Industrial Climate Scenarios

The pre-industrial climate scenarios (prefixed “uh”) use a control CO₂ concentration of 280 ppm (the concentration in the year 1870). It uses the same geography as in the PD cases, but does not account for aerosol forcings and uses a slightly lower solar constant of 1365 W/m². This scheme has a more comprehensive set of simulations with doublings of CO₂ from the control thru 5 doublings. Using this

scheme allows us to witness the evolution of temperature and the general circulation by increased concentration of CO₂. Having a continuous set of simulations makes this scheme favorable for drawing comparisons to other simulations (e.g. the Eocene climate scenarios to be addressed shortly) under similar initial conditions.

4.3 Eocene Climate Scenarios

As was mentioned previously, the Eocene climate scenarios (prefixed “EO”) use the pre-industrial CO₂ concentration as a control. The sole (but significant) difference between it and the pre-industrial simulations is the topography used. The Eocene topography is similar in structure to our present climate with a few key differences. The continents are much closer together, resulting in the Atlantic being much smaller and the Pacific Ocean being much larger. India has not yet collided with Asia to form the Himalayas, and Australia is still joined to Antarctica.

Paleoclimate proxies of tropical temperatures during this time have been estimated to be warmer than today, ranging from 28 – 32°C (*Pearson et al.*, 2001), to as high as 35 – 40°C in some regions (*Huber*, 2008). While the actual greenhouse gas (GHG) composition is hypothesized to be different than present day (*Sloan et al.*, 1992; *Beerling et al.*, 2009), our methodology to reproducing this climate is by only varying the concentration of CO₂. All other atmospheric constituents (e.g. methane) are held constant at their pre-industrial level. Similarly to the pre-industrial simulations, we have a consecutive set of simulations with increasing concentrations of CO₂ from the control thru 3 doublings.

4.4 Constant Ocean Eocene Climate Scenarios

The constant ocean Eocene climate scenarios (prefixed “kEO”) are generated from a separate coupled atmospheric-ocean model and then imposed in the constant ocean models, instead of having temperatures dynamically change within the model. This process benefits from incorporating a fully simulated ocean, but has the disadvantage of not evolving dynamically with changes in the final atmospheric model. The available outputs for these simulations run from 3 to 5 doublings of the concentration of CO₂. This scenario provides us a fairly comprehensive set of simulations using Eocene geography (although not ideal; i.e. EO0 – EO3, kEO3 – kEO5). However this does allow for comparisons among the different ocean representations. When comparing the two simulations for 3 doublings of CO₂ using Eocene geography, the constant ocean cases exhibit slightly warmer temperatures.

Figure 8 shows the climatologically averaged (a) global and (b) tropical sea surface temperature among the various model simulations. *SST* simulations using Eocene geography and 16 times the amount of CO₂ (4480 ppm) are taken to be representative of the Paleocene-Eocene Thermal Maximum (PETM) based on paleoclimate proxies (*Winguth et al.*, 2010). The PETM is a period of extreme warmth, with surface temperatures as high as 5 – 9 °C warmer than normal (*Zachos et al.*, 2005).

The exceedingly fast rate of warming during this period (for a geologic time scale) and the hypothesized amount of GHGs available is what makes the approach of examining past climates to understand future climate so appealing. The amount of atmospheric GHGs during this time is said to be analogous to the amount of total carbon

emitted from burning all of our fossil fuel reserves (*Zachos et al.*, 2008). Thus, this is a period of high interest.

5. PRESENT CLIMATE

In examining the general structure of atmospheric stability in our current climate, we find it pertinent to distinguish between land and oceanic regions. Figure 9 shows the zonally averaged climatological P^* over land and oceanic regions for the month of July. The solid black line (1.5 PVU contour) is a visual representation of the dynamical tropopause (*Hoskins et al.*, 1985). As expected, tropical lapse rates over both regions are comparable to moist adiabats, and become increasingly more stable at higher latitudes. Comparing Figures 9a & 9b gives an example of the differences among maritime and continental lapse rates. Generally, we find that marine lapse rates are relatively more stable in both its horizontal and vertical extents.

Interestingly, for the month of July, midlatitude lapse rates over land are at least neutral to moist convection throughout much of the Northern Hemisphere, showing a dominance of convection relative to stabilization by midlatitude storms. However, as can be seen in Figure 10, during January moist neutral lapse rates are confined to just beyond the boundary of the tropics. During this month, lapse rates are stable throughout much of the extratropics and the dynamic tropopause decreases in height. Thus, the thermal stratification of the atmosphere is highly dependent on the seasonal cycle.

To that regard, some interesting features present in summer months not seen in the winter are the regions of positive values of P^* at low levels and near 550 hPa. These indicate regions of stability associated with the trade wind inversion (at low levels over oceans) and the melting level (at higher altitudes over both continents and ocean). Along with increasing temperatures throughout the stratosphere, these three regions display the

trimodal characteristics found in tropical regions (*Johnson et al.*, 1999). The melting level is determined by the area where subfreezing temperatures are first encountered with height. The stable region is a direct result of melting within stratiform rain regions (*Johnson et al.*, 1996).

To better understand the implications of this cycle, we examine these changes where convection is most important. The free troposphere is an ideal location in this regard, as the changes in stability there are indicative of a parcel's behavior outside the influence of boundary layer turbulence. Furthermore, it is not only important to examine the long term averages of stability, but also how frequent atmospheric lapse rates are comparable to moist adiabats. As such, Figure 11 displays the climatological fraction of days for January and July where lapse rates are parallel to or more unstable than the moist adiabatic lapse rate through the free troposphere within an arbitrary threshold (in this case < 0.15 PVU; Korty and Schneider (2007) provides a more detailed description of its selection). As expected, there is a higher frequency of occurrence in the tropics than at higher latitudes. Interestingly, moist convection is more prevalent in the Northern Hemisphere for both seasons. The inconsistent lower frequency patches shown over some regions, such as Northern Africa in July, are a sampling error due to expansion of the boundary layer (in this case over the Sahara Desert).

It is relevant to examine the global mean circulation, in particular, the Hadley cell circulation. During the time of the spring and autumnal equinoxes, this circulation takes the form of two approximately concentric counter-rotating cells of equal magnitude with converging surface winds over the equator. The boundaries of the

individual cells coincide with the borders of the tropics. We define the Hadley cell terminus by the extension of the vertical zero contour (dashed black line) to the surface. However during the two solstice periods (Figure 12), there is a single cell with its center shifted to the hemisphere currently experiencing winter. The oscillation between its one and two-cell arrangement changes linearly with season.

A secondary approach to understanding how convective processes change with climate is to observe the changes in the stabilizing effects of midlatitude storms. A useful variable to examine these effects is the meridional heat flux caused by transient eddies: the zonal mean of the product of temporal perturbations in temperature and meridional wind speed multiplied by the specific heat capacity at constant pressure ($c_p[v'T']$). Transient eddies are an important feature in the poleward transport of temperature, moisture, and energy. Figure 13 shows the meridional heat flux caused by transient eddies for the months of January and July. Red colors are indicative of a northward transport, while bluer colors indicate a southward transport. The relative strengths of the poleward fluxes are influenced by the current season. The highest transient eddy values occur in the midlatitudes of the hemisphere experiencing winter (i.e. when the frequency of heat transporting fronts is highest).

6. DIAGNOSING LAPSE RATES IN WARMER CLIMATES

6.1 P^ Variability in a Warming Climate*

We evaluate climates of varying concentrations of CO₂, where the simulated atmosphere is allowed to thoroughly mix, until equilibrium is reached. By progressively doubling the concentrations of CO₂, we are able to record the atmospheric net forcing and changes to major climate features as described in the previous section. Figure 14 shows this temperature change for the control (335 ppm), intermediate warming (2240 ppm), and exceedingly hot (8960 ppm) climate simulations. The latter cases are representative of 8 times (3 doublings) and 32 times (5 doublings) of the pre-industrial CO₂ concentration. There appears to be non-linear temperature dependence with increased CO₂ environments, with gradual increases initially and a much stronger influence in the exceedingly hot simulation. We find that this increase not only raises the overall global temperature, but results in a weakened meridional temperature gradient. The large-scale impact of this change will be discussed in a following section.

As midlatitude weather becomes less of a dominant contributor in a warming climate, convection plays a more central role, resulting in less stable extratropical lapse rates. We see an expansion in all directions of areas where lapse rates are nearly moist adiabatic, resulting in high latitude regions exhibiting characteristics similar to the present day tropics. In the exceedingly hot simulation, it is common to find lapse rates neutral to moist convection nearly globally.

This change in globally averaged atmospheric stability is the result of a variety of changes. Generally, warmer temperatures favor parcel expansion leading to a less stable

atmospheric profile. While the model used is run to equilibrium, the magnitude of the CO₂ induced temperature changes are not realized equally throughout the globe. The amount of energy required to raise the temperature of air by a single degree increases exponentially, which results in varying increases in temperatures globally.

Therefore, in warmer climates, convection plays a more pivotal role in midlatitude regions, comparable to the tropics for our present climate. Simulations run for the Eocene epoch yield similar results; an overall increase in instability expanding from the tropics into higher latitudes with an increased global CO₂ concentration. The impact this change will have on the atmosphere for the Eocene epoch is of particular interest due to the ongoing disagreement of temperature conditions during this period. If SSTs during this period exceeded 35 °C, atmospheric conditions may have been significantly different, as proposed by Caballero and Huber (2010).

Figure 15 is similar to Figure 1a, but for P^* in an exceedingly hot climate. The white space in the figure, indicate exceedingly negative values of P^* . It shows convectively adjusted air masses throughout much of the troposphere. In addition, it shows the expansion of stable lapse rates associated with the melting level to higher altitudes (concurrent with the expansion of the 0°C isotherm). Figure 16 shows the fraction number of days that lapse rates are at least neutral to moist convection (but can be more unstable) for an exceedingly hot climate. As compared with Figure 11, we find that there is a poleward expansion of lapse rates that are frequently moist neutral. There is little change in tropical regions, showing only a slight decrease in frequency due to the sampling of the pressure levels designated as the free troposphere (700 – 400 hPa). A

warmer atmosphere yields an expanded boundary layer, which when coupled with a low level thermal inversion will show increased stability in the frequency of P^* throughout the free troposphere. Midlatitude moist neutral lapse rates become increasingly more frequent. Oceanic lapse rates in the extratropics are moist adiabatic for at least 70% of a given month, quite different to our current climate where its frequency is as low as 10%. Moreover, terrestrial lapse rates show more resistance to changes in frequency but do become more frequent in hotter climates. A more striking feature is how frequent moist convection occurs in polar regions, which is nearly unfeasible for the control case.

Examining how the seasonal variability reacts to increased CO_2 concentrations, gives insight on what the climate/day-to-day weather will be like in the future. Comparing Figures 11 & 16, we see small changes in the seasonal variability (regardless of continental or oceanic origin) with increased warming. The change in the value of P^* in January and July for the control simulation is subdued when compared to the exceedingly hot case, especially during the summertime. In contrast, winter lapse rates retain much of their original structure, with some poleward expansion of values indicating instability.

As was presented in a previous section, continental lapse rates generally tend to be more unstable when compared with maritime lapse rates. While this distinction is apparent regardless of season, it is more evident in summer months when ocean temperatures are much cooler than those on land. In warmer climate simulations, this trend is more prevalent, due to differing heat capacities of ocean water and air over land. This results in a much stronger seasonal variability in convectively neutral air masses.

6.2 Relative Magnitudes of Horizontal Components

As mentioned previously, the major benefit of using saturation potential vorticity (P^*) as a proxy for stability is that it accounts for both upright and slantwise convection. Because the value of the horizontal component of P^* is typically small, it can be treated as negligible. This assumption cannot be made, however, in strongly rotating systems such as extratropical storms and outside of the troposphere, where its value is the same order of magnitude of as upright convection.

In a previous section we provided data showing that a warmer climate state resulted in decreased stability globally, although a measure of the attributions of vertical versus horizontal components of convection was not explored. Expanding Equation 2 in pressure coordinates and applying hydrostatic balance (as shown in *Korty and Schneider, 2008*) yields:

$$P^* = -g \left[-\frac{\partial v}{\partial p} \frac{\partial \theta_e^*}{\partial x} + \frac{\partial u}{\partial p} \frac{\partial \theta_e^*}{\partial y} + (f + \zeta) \frac{\partial \theta_e^*}{\partial p} \right] \quad (3)$$

where $\zeta = \partial_x v - \partial_y u$ is the relative vorticity. The first two terms of the Equation 3 are the horizontal components of P^* , while the third (vertical component) term is essentially approximate to Ertel's dry potential vorticity.

Figure 17a depicts $-g[f + \zeta]d\theta_e^*/dp$, the sole contribution of the vertical component of P^* , for our present climate, climatologically averaged for the month of July. Comparing this result with Figure 9a (which shows the contribution by the full calculation of P^*), we verify that the vertical component of P^* is the dominating term of Equation 3. It provides the overall structure, whereas the horizontal component overall

reinforces certain areas (specifically through the free troposphere in the midlatitudes) with negative values of P^* . Figure 17b, which shows the same plot for an exceedingly hot climate, further shows this trend. Comparing the actual value of the horizontal components (not shown), shows no discernible change in magnitude among warmer climates. As was shown previously, P^* shows more negative values in warmer climates (indicative of less stable lapse rates globally). However, this change comes solely from the $-g[f + \zeta]d\theta_e^*/dp$ term, and not the horizontal term ($-g[dv/dp d\theta_e^*/dx + du/dp d\theta_e^*/dy]$).

Figure 18 depicts the fraction of days where the vertical component of P^* is representative of being moist adiabatic or more unstable through the free troposphere. By comparing this plot with Figure 11, we can examine the relative importance of the horizontal components of P^* in determining frequent moist neutral lapse rates. As with the full calculation of P^* , the highest frequencies are found in the tropics, and become less frequent farther poleward. The two plots show similar values near the equator, with larger differences at higher latitudes. This underlies the importance of the inclusion symmetric instabilities in resolving convectively adjusted air masses. Similarly, Figure 19 shows a similar plot for an exceedingly hot climate. A similar trend is found for this simulation.

6.3 Temporal Resolution Dependence of P^*

We assess how different spatial and temporal resolutions affect a models ability to reproduce P^* . We first calculate P^* from data using a 6-hourly time step, averaged for a single month, and compare with P^* calculated from daily averaged data. Figure 20

shows this for P^* generated for the first month of October from (a) 6-hourly, (b) daily averaged, and (c) the difference between the two for the control climate simulation. The two plots are comparable in structure through a majority of their vertical extent except within the boundary layer at mid to high latitudes. This difference is perpetuated in other months as well, with varying degrees of size and magnitude, but remains confined to the boundary layer. This feature, while small, is sensitive to the diurnal changes in this region. Figure 21 shows similar results, this time for an exceedingly hot climate. This shows that to a good degree, calculating P^* from 6-hourly averaged data versus daily averaged data provides similar results. As the use of high temporal resolution model data is not always a readily available option, we find this to be an encouraging result.

7. HADLEY CELL CIRCULATION AND TRANSIENT EDDIES

Another important feature examined was the Hadley cell circulation. As was shown in section 2, this circulation goes through a yearly oscillation between a strong northern hemisphere cell, two equal magnitude cells divided along the equator, and a strong southern hemisphere cell. Examining changes in this feature is important because it is a major influence on the strength and breadth of tropical meteorology.

Figure 22 depicts streamlines that show the circulation for an exceedingly hot climate for the month of January (32 times the pre-industrial concentration of CO_2). Comparing these plots with Figure 12 shows that the magnitude of the circulation has roughly stayed the same. In actuality, there is a slight increase in its strength at its core with in the intermediate warming case, and a subsequent weakening in the exceedingly hot case. However, this change is minimal and would not have any significant impact on the atmosphere

However, the extension of the Hadley cell terminus to higher latitudes could have significant impacts on both weather and climate. In Figure 22, we find that for the July simulation, the northern extent of the Hadley cell shifts when compared with its control case. The change in the location of its northern boundary shows little change within the initial doublings of CO_2 , but is much more apparent in the warmest climate scenarios. This could possibly be why the strength of the circulation increases with warming and then decreases as it extends over larger distances.

The expansion of the Hadley cell would have many repercussions on the general circulation. Its descending branches create surface level divergence and acts as a natural

barrier to tropical convection, while ascending branches create surface level convergence and lift. Displacement of these extents well outside of the tropics and into midlatitude regions ($\sim 40^\circ\text{N}$), shifts the location of the subtropical jet and extends the regions to where tropical meteorology can occur. Surface air moving from higher latitudes to the equator associated with the Hadley cell, are deflected to the right (left) in the Northern (Southern) Hemisphere. Therefore, displacement of the Hadley cell terminus introduces easterlies in regions that experience westerlies in our present climate. The height of the tropopause increases as the atmosphere is warmed. This affects the Hadley cell circulation by stretching its vertical extent while maintaining its strength.

One of the more indicative features of how significant convective processes become in a warming climate, is to consider the importance of large-scale processes, such as fronts associated with midlatitude cyclones. Overall, as was shown in previous sections, environmental lapse rates become more unstable. The direct increase in temperature is a motivating factor but there are other important indirect effects such as the weakening of the meridional temperature gradient. The large imbalance of heat between equator and pole regions is what drives large-scale weather. Any alteration to this process changes the role of weather in climate. As the meridional temperature gradient weakens, large-scale weather is less favorable to occur.

Figure 23 shows the strength of the transient eddy heat flux in an exceedingly hot climate for the months of January and July. Comparing with Figure 13, we notice a significant decrease in its strength for both months by about 50%. This decrease is indicative of a weakening meridional transport of heat by large-scale weather, resulting

in less frequent stabilizing effects of midlatitude cyclones on the atmosphere. This change lessens the relative significance midlatitude weather has on atmospheric stability.

In warmer climates, convective processes become the more influential process on atmospheric stability in the extratropics, similar to present day tropical regions. This explains why P^* values (and hence instability) increase by as much as was shown in Figure 15. In conjunction with differential increases in temperature at the surface and tropopause, the lack of frequent stabilizing extratropical storms leads to the relative increase in instability.

8. SOUNDINGS AND MIDLATITUDE STORM TRACKS

An alternate approach in understanding how sensitive lapse rates are to a warming climate is examining the environmental profile at a single location (within the limitations of the model resolution) or averaged over a particular region (i.e. the continental U.S., North Pacific Ocean, etc.). Using this method has the advantage of being able to see how a typical parcel of air reacts in an environment conducive to convection. It also gives a visual representation of temperature changes to the upper atmosphere and height of the tropopause (the implications of which will be explored later in this section).

Figures 24a & 24b show the climatologically averaged extratropical lapse rate for the month of July in the Northern Hemisphere over land and ocean for 3 different concentrations of CO₂. Surface temperatures increase dramatically to unprecedented levels, progressively through the cases, accompanied by a more unstable profile in the exceedingly hot case. As expected, the height of the tropopause (visually, the point on the sounding where the temperature is isothermal with height) extends higher with increased CO₂ concentrations. A more striking feature is the relatively small change in tropopause temperature change accompanying this increase in height. This shows that while a warming climate does exhibit large increases in sea surface temperatures globally, changes at higher altitudes are much smaller.

The implications of this type of change in temperature distribution are similar to those that were described with the changes in P^* . That is, a stronger vertical temperature gradient would lead to an imbalance of surface heat, and result in an increased frequency

of convection. It has been suggested (*Bister and Emanuel et al.*, 2002; *Emanuel and Solomon et al.*, 2013) that models under predict temperature change at the tropopause (due to warming by major volcanic eruption, ozone depletion or increased Brewer–Dobson upwelling). They found that temperatures at this altitude decrease, furthering the difference in surface and tropopause temperatures.

The thermal tropopause is created by first using a cubic spline interpolation scheme on the vertical components of temperature. From the interpolated data, we generate the thermal profile and find where lapse rates begin to increase with height. Examining the entire column of available data filters out thermal inversions and occurrences of multiple tropopause. Figure 25 shows the climatologically averaged tropopause temperature for the month of July under present day concentrations of CO₂. Bluer colors are indicative of a cooler (higher) tropopause, while more red colors show a warmer (lower) tropopause. The expansion of warmer surface air, as seen in the tropics, causes the tropopause to occur at higher elevations. The coldest temperatures occur in the tropics, with warmer temperatures farther poleward. It's also worth noting that the hemisphere experiencing winter has colder tropopause temperatures.

A strong vertical temperature gradient is indicative of, as well as necessary for, deep convection. Figure 26 shows the climatologically averaged temperature difference between the sea surface and tropopause for the control case. We see a similar trend as was shown for SSTs and thermal tropopause. The largest difference is confined to the tropics by the descending branches of the Hadley cell circulation and decreases farther poleward.

In comparison, this difference under the exceedingly hot climate simulation (Figure 27) is similar in structure in the tropics to the control case, although with slightly higher values throughout. The highest values extend poleward, still bounded by the expanded Hadley cell circulation. However, dissimilarities between the cases occur outside of the tropics, where strong vertical temperature gradients are present in polar regions. These enhanced gradients are not seen in our present climate, as shown in Figure 11, where moist neutral lapse rates occur very infrequently at high latitudes.

This disparity in temperature is especially significant to the potential intensity of tropical cyclones (TC) and midlatitude storm tracks. A large vertical temperature gradient through the core of a tropical cyclone is necessary for enhancement. Therefore, because in warmer climates the number of regions conducive to such strong gradients is increasing, we demonstrate that storm intensity within those regions will be enhanced. A metric to describe this process was introduced (e.g., *Bister and Emanuel, 1998*) using only a few variables, making it a useful tool to be used in modeling and parameterization.

Maximum Potential Intensity (*MPI*) is an index of the purely thermodynamic maximum intensity a tropical cyclone can attain. To put more simply, it is the theoretical speed limit of a tropical cyclone's angular speed. *MPI* is thus defined as:

$$MPI = \sqrt{\frac{C_k}{C_d} \frac{SST - T_o}{T_o} (k^* - k)} \quad (4)$$

where C_k and C_d are the exchange coefficients for enthalpy and drag respectively, k^* is the saturation enthalpy of the sea surface, and k is the enthalpy of the boundary layer. In

our analysis, we take the C_k/C_d term to have a constant value of 0.9, which lies within the modeled threshold found in Emanuel (1995). In addition, while the k^* and k terms do show some appreciable regional variability, it is the differential temperature term that is crucial in the creation of very high values of intensity. A large value for this term, where SST is the temperature at the sea surface and T_o is the outflow temperature, represents a diverse vertical thermal gradient. The outflow temperature is the temperature at the level where upper level divergence associated with ascending air reaching a stable air mass occurs. Typically this temperature is well associated with the tropopause temperature, although some differences can occur. Due to cooling that can occur in the stratosphere, the tropopause temperature may actually be colder. Recent studies (*Emanuel and Solomon et al.*, 2013) examine how this change has contributed to the enhancement of some Atlantic Hurricane activity periods over the past few decades.

Figure 28 shows the plot of maximum monthly averaged MPI for our current climate. The red colors are indicative of regions of high MPI , while bluer colors indicate regions of a low MPI . The regions of highest intensity lie within the tropics, particularly in the Pacific and Indian Oceans, in both hemispheres. There is a sharp gradient in MPI values corresponding with the location of the descending branch of the Hadley cell circulation. Strong upper level convergence pushes cold air downwards to the surface, decreasing $SSTs$ and therefore the magnitude of MPI . The existence of tropical cyclones located outside of this region, where thermal profiles are stable to deep convection and values of $MPI < 20$ m/s, is not feasible.

Beyond using *MPI* as an index for storm intensity, it can also be used as a diagnostic for deep convection. *MPI* exceeds 55 m/s, for example, only where soundings permit convection to penetrate to the upper troposphere (*Korty et al.*, 2011). Examining the plot, we see a value of 55 m/s only appears within the bounds of the tropics, having exclusively weaker values outside of this region. This agrees with the fact that, in our current climate deep convection is not the single determinant of the thermal structure of the extratropics. However, we will find that using this diagnostic will give insight on convection's role in future climates.

Figure 29 shows a plot of *MPI* for the case where CO_2 concentrations equal to 8 times (2240 ppm) the pre-industrial amount. Many similarities exist between it and Figure 28. The most intense regions still lay within the confines of the tropics, though most of the values contained have increased in magnitude. This increase in intensity is concurrent with the strengthening of the vertical temperature gradient throughout the region. Another significant distinction between the two cases is the slight poleward expansion of regions where tropical cyclones are realistically expected to reside. As was shown in Figure 22, this corresponds with the expansion of the Hadley cell. Because its terminus is located at a higher latitude, the Hadley cell allows storm tracks to extend to regions not feasible in our current climate.

The vertical extent of a tropical cyclones core is often large enough that its outflow temperature is roughly equal to the temperature at the tropopause. It is this temperature, as was shown in Figure 24, that doesn't undergo any appreciable changes,

while sea surface temperatures increased by as much as 10 - 20 °C. The resulting thermal structure is one that is favorable for the intensification of tropical cyclones.

Figure 30 depicts *MPI* for an exceedingly hot climate. It is reasonable to suggest that *MPI* values for this climate have progressed in the same way as the preceding case, relative to the control. More regions are able to accommodate more intense storms globally and there is a large poleward shift of the largest *MPI* values outward from the tropics and into midlatitude regions bounded by the expanded Hadley cell circulation. A key feature, however, is the inclusion of relatively high *MPI* values beyond the Hadley cell terminus.

It is worth reiterating that the intensity of a TC is dependent on the thermal column it resides in (i.e., not exclusively on sea surface temperature). It is often stated that a minimum *SST* of 26° C is necessary for hurricane formation, however this is an over simplification of the necessary thermodynamic conditions. A correlation between high temperatures and hurricane does in fact exist; however, recent research has shown (Cathey, 2011) that this correlated minimum temperature increases in warmer climates. The temperatures found at the tropopause, however, bind this correlation.

For a climate where CO₂ concentrations are as high as 32 times the amount of pre-industrial concentrations, sea surface temperatures, in some polar regions can be as high as 35 °C. In conjuncture with minimal changes in tropopause temperature, this thermal structure permits the sustainment of TC's in polar regions for the northern hemisphere.

Given the necessary environmental conditions are met, arctic hurricanes can occur in our present climate (*Emanuel and Rotunno, 1989*). This type of hurricane occurs only when warm core polar lows reside in unstable environments, which is uncommon. Contrasting, for an exceedingly hot climate, Figure 30 shows polar regions in the northern hemisphere conducive to moderately intense tropical cyclones averaged over a given month.

Taking an averaged sounding over a polar region of high values of *MPI* (Figure 31) we can see the evolution of the thermal structure through the different climate scenarios. The control and intermediate warming cases show low level stability and low tropopause heights (both common throughout the arctic in our present climate). Through the free troposphere lapse rates are stable for the control case and nearly neutral for the intermediate warming case. The tropopause temperature for the two cases is similar all the while tropopause height has increased. The averaged sounding in the exceedingly hot climate case is moist neutral throughout the free troposphere. Interestingly, the tropopause temperature in this scenario decreases relative to previous cases.

Figure 32 shows the climatologically averaged temperature difference between sea surface and tropopause over the same region. There is a gradual change between the control and intermediate warming cases, followed by a more pronounced increase in the exceedingly hot climate scenario. The transformation of polar maritime regions from having stable lapse rates in our present climate to being convectively adjusted in the exceedingly hot climate scenario is a major contributor to the high values of *MPI* shown in Figure 30.

It is important to note that this index is based solely on thermodynamic variables. As such, it shows the absolute maximum potential for hurricane intensity under ideal dynamic circumstances. Various other factors conditions such as vertical wind shear, moist entropy, convergence, and the general circulation play an important and necessary role (Riehl, 1948; Bergeron, 1954; Gray, 1979) in the genesis and sustainability of TCs in these areas. The scope with which we examine intense TC's is how conducive a particular climate is to high values of *MPI*, and not in individual storms. As such, the resolution of the data, although not particularly fine, is satisfactory for this application.

8.1 Implications of a Warming Climate

The compilation of these changes and those on the general circulation presented previously create an environment quite different than what we experience today. The implications of increased convectively neutral air masses globally result in less stable poles, tropical conditions in midlatitudes, and tropical regions becoming more dry and arid. This effectively shifts the location of storm tracks farther poleward and therefore the regions receiving the highest amount of rain annually. This greatly affects industries which are highly dependent on the regional climatology, such as the growth of crops in agriculture or the maintaining of certain species of animals. Even the temperatures in the intermediate warming scenario are warm enough to yield an environment without ice.

Concurrent with the overall increase in temperature, higher concentrated CO₂ environments yield a weakened meridional temperature gradient. This feature is of particular importance in both the creation and maintenance of heat fluxes by transient

eddies. Its weakening results in less frequent extratropical storms (and thus the associated fronts that transport heat). While the type of climate change discussed thus far is a gradual change, preparations must be made for any ensuing environmental conditions.

9. EOCENE AND PRE-INDUSTRIAL SCENARIO DIFFERENCES

As mentioned in a previous section, one of the main motivations for studying climates under exceedingly high concentrations of CO₂ is the association made between warming during the PETM to the warming trend seen currently. The general atmospheric and thermodynamic differences found between pre-industrial (lower solar constant but does not include the effects of aerosol forcings) and present day simulations are subtle. Changes between schemes involving Eocene geography and those presented previously are a bit more complex. Because the only difference in the prescribed conditions between pre-industrial and Eocene simulations is the geography, we explore their model result consistencies now.

Figure 33 shows a comparison of the fraction of days for where lapse rates are at least moist adiabatic through the free troposphere for both an Eocene and pre-industrial intermediate warming climate scenario. The two plots show a similar arrangement of frequency throughout the tropics but differ at higher latitudes. For both January and July, the Eocene simulation tends to have a higher frequency of moist neutral lapse rates, especially in the Northern Hemisphere. The region just west of modern day Greenland, for example, experiences a convectively adjusted air mass ~40% during the month of July for the pre-industrial case, while being as high as ~80% in the Eocene simulation. This distinction alone would yield vastly different local climate conditions.

Figure 34 shows the climatologically averaged July zonal circulation using Eocene and Pre-industrial climate conditions under an intermediate warming scenario. The two circulations show some similarities in structure but vary in magnitude. The

Eocene simulation has a relatively weaker Hadley cell circulation, while its horizontal and vertical boundaries remain similar. One important feature present in the Eocene simulation is the (albeit weak) northern hemisphere counter-rotating cell coupled with the dominant southern cell, similar to the “typical” Hadley cell configuration. The inclusion of this southern cell, specifically its northern descending branch, results in cooler surface temperatures, absent in the present day simulations.

Likewise, a comparison of the meridional heat flux caused by transient eddies between the Eocene and pre-industrial scheme is presented in Figure 35 for the month of July. Distinctions among the heat flux for two schemes aren’t nearly as obvious. They both include strong winter transport of heat, similar in both magnitude and structure. Summer meridional heat transport by transient eddies is slightly weaker in the simulation running Eocene topography.

Interestingly, *SSTs* are found to be higher globally in the Eocene simulations (Table 1) by $\sim 3^{\circ}\text{C}$ consistently among the various simulations, even with a stronger surface divergence in the northern hemisphere tropics caused by the Hadley cell. However, one key feature unique to schemes using present day geography, absent from the Eocene runs, is the increase in summer Northern Hemisphere *SSTs* at high latitudes. With each successive doubling of CO_2 this increase is compounded. This feature is a major contributor to the diverse vertical temperature profile and the sustainment of intense tropical cyclones (as shown in Figure 30). Void of this characteristic, the Eocene simulations do not yield arctic hurricanes regardless of CO_2 concentration. Figure 36 shows the resultant *MPI* under this scenario.

There is a two-part explanation for the dissimilarities shown between Figures 30 & 36. Firstly, the calculation of *MPI* from model data using prescribed *SSTs* is subject to errors. While they are generated from a coupled atmospheric-ocean model, the *SSTs* do not evolve within the model, which can lead to spurious surface energy fluxes. Because *MPI* is highly sensitive to the surface energy budget, any values computed from model output run with imposed *SSTs* should be viewed with caution. Secondly, the decrease in strength of the meridional heat flux by transient eddies in the Eocene simulations for an exceedingly hot climate is comparable to those found using present day topography (Figure 23). Thus, the dominant mechanism for heat transport becomes the ocean, which is ineffective at high latitudes in the Northern Hemisphere due to the basin cutoff in the Eocene geography.

10. CONCLUSIONS

This thesis examined how the thermal stratification of the troposphere changes in simulations forced by high levels of carbon dioxide. Our results show that a CO₂ induced warming causes a variety of changes to the general circulation and the overall makeup of climate. In our present climate, both convective processes and the stabilizing effects of extratropical storms affect the extratropical lapse rates. In simulations of warmer climates in which the meridional temperature gradient is weakened, less frequent storms cause the lapse rate to be sustained almost entirely by convective processes, similar to the tropics in our current climate.

This study uniquely considers convective motions that respond to both gravitational accelerations as well as symmetric instabilities. By calculating a moist variant of potential vorticity, we identified regions where the saturation entropy is constant or decreases along angular momentum surfaces. In nature (and in models where this process is parameterized), a decrease along this slanted path is unstable, and a convective adjustment ensues.

We assessed the ability of current models to resolve conditions unstable to slantwise convection by examining reanalysis data of cases in which slantwise convection was observed and reported in the published literature. Using saturation potential vorticity, we are able to reproduce observations of slantwise convective instability for the cases reported by Emanuel (1988) in reanalysis products of varying resolutions. We showed that even the coarsest resolution model (NCEP/NCAR: $\sim 2.5^\circ \times 2.5^\circ$) is able to capture these instances of slantwise convection fairly well. Our results

suggest that model parameterizations of convection should include the ability to realize instabilities arising from symmetric displacements. Each of the case studies show signatures of stable lapse rates in the vertical direction, while being conditionally unstable along slanted M -surfaces.

In addition to overall increased temperatures and instability of lapse rates, changes to the Hadley cell circulation occur as well. While our results show that the cell doesn't have any substantial changes in strength when comparing the control and exceedingly hot climate simulations, the location of its terminus occurs at higher latitudes in warmer climates. This expansion allows tropical weather (and thus the region of descending cold air) to occur in regions that it currently cannot. The specific location of the Hadley cell continues its correlation with season, while slightly favoring a single-cell structure.

In response to rising CO₂ levels, sea surface temperatures increase across the range of simulations and the vertical profiles tethered to them become less stable over the extratropics. This results in a deeper troposphere with higher altitude tropopause, though the temperature at the upper boundary remains largely similar across the wide range of climates. Some areas, such as Northern Hemisphere polar regions, show a decrease in temperature. Heights of the tropopause do indeed increase due to thermal expansion, resulting in deep, strong vertical temperature gradients, necessary for deep convection. Meeting this criterion, coupled with the increase in regions of tropical meteorology, is the foundation for tropical cyclones genesis and sustainment.

One consequence of these changes is that the Maximum Potential Intensity of tropical cyclones, which today is capped in extratropics by thermal profiles stable to deep convection, rises in the hottest simulations at all latitudes. We found a strong correlation between the expansion of the Hadley cell terminus with the number of regions conducive to intense hurricane sustainment. These regions show increases in intensity to a certain degree, but do not surpass an intrinsic threshold (~ 100 m/s). Thus, while our results show no indications of any changes in tropical cyclone frequency under warmer environmental conditions, the number of regions conducive to the most intense storms does increase. Plots of maximum potential intensity under exceedingly hot climate conditions yielded results of sustainment of arctic hurricanes.

Comparisons between Eocene and pre-industrial simulations provided insight on the effect of topography on lapse rates and the general circulation. Global SSTs were found to be higher in Eocene simulations, concurrent with a higher frequency of moist neutral lapse rates. Both the Hadley cell circulation and the meridional heat flux by transient eddies showed similar results among Eocene and pre-industrial simulations. Eocene topography blocking ocean heat transport to high latitudes in the Northern Hemisphere, and a weakening transient eddy heat flux in the exceedingly hot climate simulation, results in cooler temperatures insufficient for arctic hurricane sustainment.

REFERENCES

- Alduchov, O. A., and R. E. Eskridge, 1996: Improved magnus form approximation of saturation vapor pressure. *J. Appl. Meteor.*, **35**, 601–609.
- Barry, L., G. C. Craig, and J. Thuburn, 2000: A gcm investigation into the nature of baroclinic adjustment. *J. Atmos. Sci.*, **57**, 1141–1155.
- Beerling, D. J., R. A. Berner, F. T. Mackenzie, M. B. Harfoot, and J. A. Pyle, 2009: Methane and the CH₄-related greenhouses effect over the past 400 million years, *Amer. J. Sci.*, **309**, 97–113.
- Bennetts, D. A., and B. J. Hoskins, 1979: Conditional symmetric instability – A possible explanation for frontal rainbands. *Quart. J. Roy. Meteor. Soc.*, **105**, 945–962.
- Bergeron, T., 1954: The problem of tropical hurricanes. *Quart. J. Roy. Meteor. Soc.*, **80**, 131–164.
- Betts, A. K., 1982: Saturation point analysis of moist convective overturning. *J. Atmos. Sci.*, **39**, 1484–1505.
- Bister, M., and K. A. Emanuel, 1998: Dissipative heating and hurricane intensity. *Meteor. Atm. Phys.*, **52**, 233–240.
- Bister, M., and K. A. Emanuel, 2002: Low frequency variability of tropical cyclone potential intensity, 1, Interannual to interdecadal variability, *J. Geophys. Res.*, **107**(D24), 4801.
- Buck, A. L., 1981: New equations for computing vapor pressure and enhancement factor. *J. Appl. Meteor.*, **20**, 1527–1532.

Caballero, R., and M. Huber, 2010: Spontaneous transition to superrotation in warm climates simulated by CAM3. *Geophys. Res. Lett.*, **37**, L11701.

Cathey, S. C., 2011: ‘Tropical cyclone genesis factors in a warming climate’, Masters Thesis, Texas A&M University.

Emanuel, K. A., 1983a: The lagrangian parcel dynamics of moist symmetric instability. *Mon. Wea. Rev.*, **111**, 2016–2033.

Emanuel, K. A., 1983b: On assessing local conditional symmetric instability from atmospheric soundings. *Mon. Wea. Rev.*, **111**, 2016–2033.

Emanuel, K. A., 1988: Observational evidence of slantwise convective adjustment. *Mon. Wea. Rev.*, **116**, 1805–1816.

Emanuel, K. A., 1994: *Atmospheric Convection*. Oxford University Press, 580.

Emanuel, K. A., 1995: Sensitivity of tropical cyclones to surface exchange coefficients and a revised steady-state model incorporating eye dynamics. *J. Atmos. Sci.*, **52**, 3969–3976.

Emanuel, K. A., 2007: Quasi-equilibrium dynamics of the tropical atmosphere. *The Global Circulation of the Atmosphere*, Schneider, T. and A. H. Sobel, editors, Princeton University Press, 385.

Emanuel, K. A., 2008: Back to Norway. *Sanders Symposium Monograph, Meteor. Monogr.*, No. 55, Amer. Meteor. Soc.

Emanuel, K. A., and R. Rotunno, 1989: Polar lows as arctic hurricanes. *Tellus*, **41A**, 1–17.

Emanuel, K. A., R. Sundararajan, and J. Williams, 2008: Hurricanes and global warming: results from downscaling IPCC AR4 simulations. *Bull. Amer. Meteor. Soc.*, **89**, 347–367.

- Emanuel, K. A., S. Solomon, D. Folini, S. M. Davis, and C. Cagnazzo, 2013: Influence of tropical tropopause layer cooling on atlantic hurricane activity, *J. Climate*, **26**, 2288–2301.
- Frisius, T., 2005: A balanced model of an axisymmetric vortex with zero potential vorticity. *Tellus A*, **57**, 55–64.
- Gray, W. M., 1979: Hurricanes: Their formation, structure and likely role in the tropical circulation. *Meteorology Over Tropical Oceans*, Shaw, D. B., editor, Royal Meteorological Society, 155–218.
- Gutowski, W. J., 1985: Baroclinic adjustment and midlatitude temperature profiles. *J. Atmos. Sci.*, **42**, 1733–1745.
- Gutowski, W. J., L. E. Branscorne, and D. Stewart, 1989: Mean flow adjustment during life cycles of baroclinic waves. *J. Atmos. Sci.*, **46**, 1724–1737.
- Gutowski, W. J., L. E. Branscome and D. Stewart, 1992: Life cycles of moist baroclinic eddies. *J. Atmos. Sci.*, **49**, 306–319.
- Held, I. M., 1982: On the height of the tropopause and the static stability of the troposphere. *J. Atmos. Sci.*, **39**, 412–417.
- Hoskins, B. J., M. E. McIntyre, and A. W. Robertson, 1985: On the use and significance of isentropic potential vorticity maps. *Quart. J. Roy. Meteor. Soc.*, **111**, 877–946.
- Huber, M., 2008: A hotter greenhouse?. *Science*, **321**, 353–354.
- Juckes, M. N., 2000: The static stability of the midlatitude troposphere: The relevance of moisture. *J. Atmos. Sci.*, **57**, 3050–3057.
- Johnson, R. H., P. E. Ciesielski, and K. A. Hart, 1996: Tropical inversions near the 0°C level. *J. Atmos. Sci.*, **53**, 1838–1855.

- Johnson, R. H., T. M. Rickenbach, S. A. Rutledge, P. E. Ciesielski, and W. H. Schubert, 1999: Trimodal characteristics of tropical convection. *J. Climate*, **12**, 2397–2418.
- Korty, R. L., S. J. Camargo, and J. Galewsky, 2012: Tropical cyclone genesis factors in simulations of the Last Glacial Maximum. *J. Climate*, **25**, 4348–4365.
- Korty, R. L., and T. Schneider, 2007: A climatology of the tropospheric thermal stratification using saturation potential vorticity. *J. Climate*, **20**, 5977–5991.
- Lindzen, R. S., 1993: Baroclinic neutrality and the tropopause. *J. Atmos. Sci.*, **50**, 1148–1151.
- Lindzen, R. S., B. Farrell, and K.-K. Tung, 1980: The concept of wave over-reflection and its application to baroclinic instability. *J. Atmos. Sci.*, **37**, 44–63.
- North, G. R., 1975: Theory of energy-balance climate models. *J. Atmos. Sci.*, **32**, 2033–2043.
- Pearson, P. N., P. W. Ditchfield, J. Singano, K. G. Harcourt-Brown, C. J. Nicholas, R. K. Olsson, et al. 2001: Warm tropical sea surface temperatures in the late cretaceous and eocene epochs, *Nature*, **441**, 610–613.
- Phillips, N. A., 1954: Energy transformations and meridional circulations associated with simple baroclinic waves in a two-level, quasi-geostrophic model. *Tellus*, **6**, 273–286.
- Riehl, H., 1948: On the formation of typhoons. *J. Meteor.*, **5**, 247–264.
- Reuter, G. W., and M. K. Yau, 1990: Observations of slantwise convective instability in winter cyclones. *Mon. Wea. Rev.*, **118**, 447–458.
- Schneider, T., 2007: The thermal stratification of the extratropical troposphere. *The Global Circulation of the Atmosphere*, T. Schneider and A. H. Sobel, editors, Princeton University Press, 47–77.

Showstack, R., 2013: Carbon dioxide tops 400 ppm at Mauna Loa, Hawaii, *Eos Trans. AGU*, **94**(21), 192.

Simmons, A. J., A. Untch, C. Jakob, P. Kållberg, and P. Undén, 1999: Stratospheric water vapour and tropical tropopause temperatures in ECMWF analyses and multi-year simulations. *Quart. J. Roy. Meteor. Soc.*, **125**, 353–386.

Sloan, L. C., J. Walker, T. C. Moore, D. Rea, and J. C. Zachos, 1992: Possible methane-induced polar warming in the early Eocene, *Nature*, **357**, 320–322.

Stone, P. H., 1978: Baroclinic adjustment. *J. Atmos. Sci.*, **35**, 561–571.

Stone, P. H., and B. Nemet, 1996: Baroclinic adjustment: A comparison between theory, observations, and models. *J. Atmos. Sci.*, **53**, 1663–1674.

Stone, P. H., and J. H. Carlson, 1979: Atmospheric lapse rate regimes and their parameterization. *J. Atmos. Sci.*, **36**, 415–423.

Tetens, V. O., 1930: Über einige meteorologische Begriffe. *Zeitschrift für Geophysik.*, **6**, 297–309.

Winguth, A., C. Shellito, C. Shields, and C. Winguth, 2010: Climate response at the paleocene-eocene thermal maximum to greenhouse gas forcing – A model study with CCSM3. *J. Climate*, **23**, 2562–2584.

Xu, K., and K. A. Emanuel, 1989: Is the tropical atmosphere conditionally unstable?. *Mon. Wea. Rev.*, **117**, 1471–1479.

Zachos, J. C., G. R. Dickens, and R. E. Zeebe, 2008: An early Cenozoic perspective on greenhouse warming and carbon-cycle dynamics. *Nature*, **451**, 279–283.

Zachos, J. C., U. Röhl, S. A. Schellenberg, A. Sluijs, D. A. Hodell, D. C. Kelly, E. Thomas, M. Nicolo, I. Raffi, L. J. Lourens, H. McCarren, and D. Kroon, 2005: Rapid acidification of the ocean during the Paleocene-Eocene Thermal Maximum. *Science*, **308**, 1611–1615.

APPENDIX A

SATURATION EQUIVALENT POTENTIAL TEMPERATURE

Saturation potential vorticity (P^*) is defined similarly to Ertel's potential vorticity (P), replacing potential temperature (θ) with saturation equivalent potential temperature (θ_e^*). θ_e^* is defined as the potential temperature a parcel would have if it was both saturated and all the contained water vapor was condensed, releasing its latent heat. It is derived from the saturation vapor pressure (e^*), which we calculate from Tetten's formula (Teten, 1933):

$$e^*(T) = 6.1121 \cdot \exp\left(a_3 \frac{T - T_0}{T - a_4}\right) \quad (\text{A1})$$

where the precise values of the coefficients a_3 and a_4 are dependent on temperature.

Coefficients depicting saturation over liquid water for temperatures above $T_0 = 273.16$ K are those presented in Buck (1981), while those occurring over ice for temperatures below $T_i = 250.16$ K are taken from Alduchov and Eskridge (1996). Intermediate temperatures between these two thresholds depicting a mixed phase composition (Simmons *et al.*, 1999) are given by:

$$e^*(T) = e_i^*(T) + \left(e_w^*(T) - e_i^*(T)\right) \left(\frac{T - T_i}{T_0 - T_i}\right)^2 \quad (\text{A2})$$

where e_w^* and e_i^* are the saturation vapor pressures calculated from Equation A1 using coefficients for those over water and ice, respectively. Using this value we calculate the saturation mixing ratio (r^*):

$$r^* = \frac{R_d}{R_v} \frac{e^*}{p - e^*} \quad (\text{A3})$$

We then calculate the latent heat of vaporization (L_v) for temperatures above T_0 by the formula:

$$L_v = L_{v0} - (c_{pl} - c_{pv})(T - T_0) \quad (\text{A4})$$

where the latent heat of vaporization at the triple point $L_{v0} = 2.501\text{E6 J/kg}$; c_{pl} and c_{pv} are the heat capacities of liquid water and water vapor, respectively. We take the latent heat of sublimation (L_s) to have a constant value of 2.501E6 J/kg for temperatures less than T_i . Taking this value to be constant will be correct within an error of ± 0.01 for the given temperatures. Latent heats in between vaporization and sublimation are calculated in a similar manner following Equation A2:

$$L(T) = L_s + (L_v(T) - L_s) \left(\frac{T - T_i}{T_0 - T_i} \right)^2 \quad (\text{A5})$$

Finally we are able to use our calculated values of L and r^* in the formula for saturation equivalent potential temperature:

$$\theta_e^* = T \left(\frac{p_0}{p_d} \right)^{R_d / (c_{pd} + c_l r_t)} \exp \left[\frac{L r^*}{(c_{pd} + c_l r_t) T} \right] \quad (\text{A6})$$

where p_0 is a reference pressure (1000 hPa); p_d is the partial pressure of dry air; R_d is the gas constant for dry air; R_v is the gas constant for water vapor; c_{pd} is the heat capacity for dry air; and r_t is the total mixing ratio (which will equal r^* in our calculations since we do not consider liquid water content r_l in our analysis).

APPENDIX B

TABLES

Simulation Name	CO₂ Concentration	Global Averaged SST	Number of Available Years: Monthly Data	Number of Available Years: 6-Hourly Data
uhPD	355 ppm	17.14 °C	25	17
uhPD3	2240 ppm	22.88 °C	19	19
uhPD5	8960 ppm	33.69 °C	19	18
uh0	280 ppm	15.01 °C	20	18
uh1	560 ppm	18.27 °C	70	41
uh2	1120 ppm	20.34 °C	24	22
uh3	2240 ppm	23.01 °C	21	18
uh4	4480 ppm	26.57 °C	24	25
uh5	8960 ppm	33.18 °C	15	14
EO0	280 ppm	20.28 °C	61	24
EO1	560 ppm	23.29 °C	10	10
EO2	1120 ppm	23.01 °C	47	37
EO3	2240 ppm	25.11 °C	32	31
kEO3	2240 ppm	26.42 °C	73	---
kEO4	4480 ppm	29.32 °C	55	26
kEO5	8960 ppm	36.74 °C	33	30

Table 1: Climatologically averaged global sea surface temperature for different model simulations. The simulation naming convention uses the prefix “uh” to refer to a scheme of climate simulations that reach ultra hot temperatures, and “PD” to refer to the use of present day topography. The numerical suffix denotes the amount of doublings of the pre-industrial concentration of CO₂. The names of the simulations prefixed with “uhPD” use a control case CO₂ concentration of 355 ppm, fixed solar constant of 1367 W/m², fixed ocean heat transport, is coupled to a slab ocean, and includes aerosol forcings. Simulations prefixed only by “uh” differ by using a control case CO₂ concentration of 280 ppm, a slightly lower solar constant of 1365 W/m² and do not include aerosol forcings. Simulation names prefixed with “EO” use similar conditions to those prefixed only by “uh” but uses topography representative of the Eocene epoch. Simulation names prefixed by “kEO” differ from “EO” simulations by using imposed sea surface temperature values instead of a slab ocean.

APPENDIX C

FIGURES

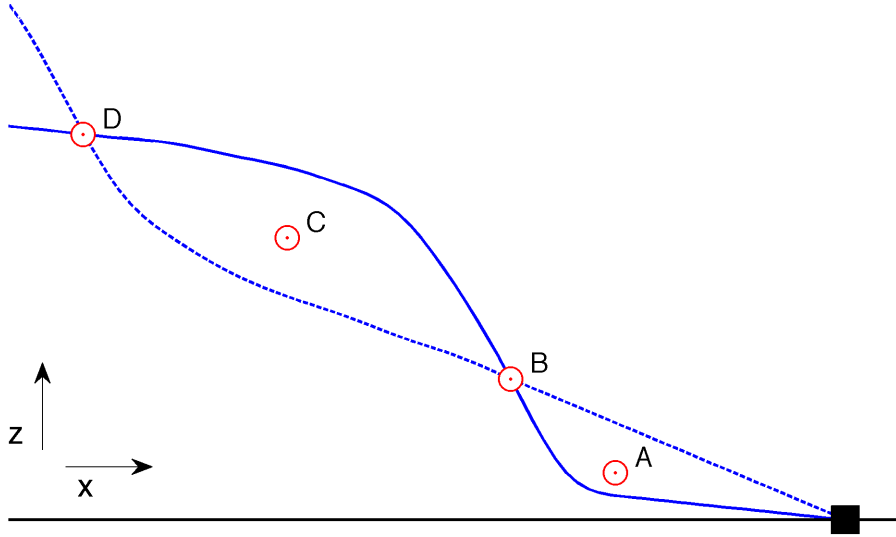


Figure 1: Isolines of saturation equivalent potential temperature (θ_e^* ; solid line) and angular momentum (M ; dashed line). Both have increasing values in the positive x and z-directions. The square denotes a theoretical parcel of air.

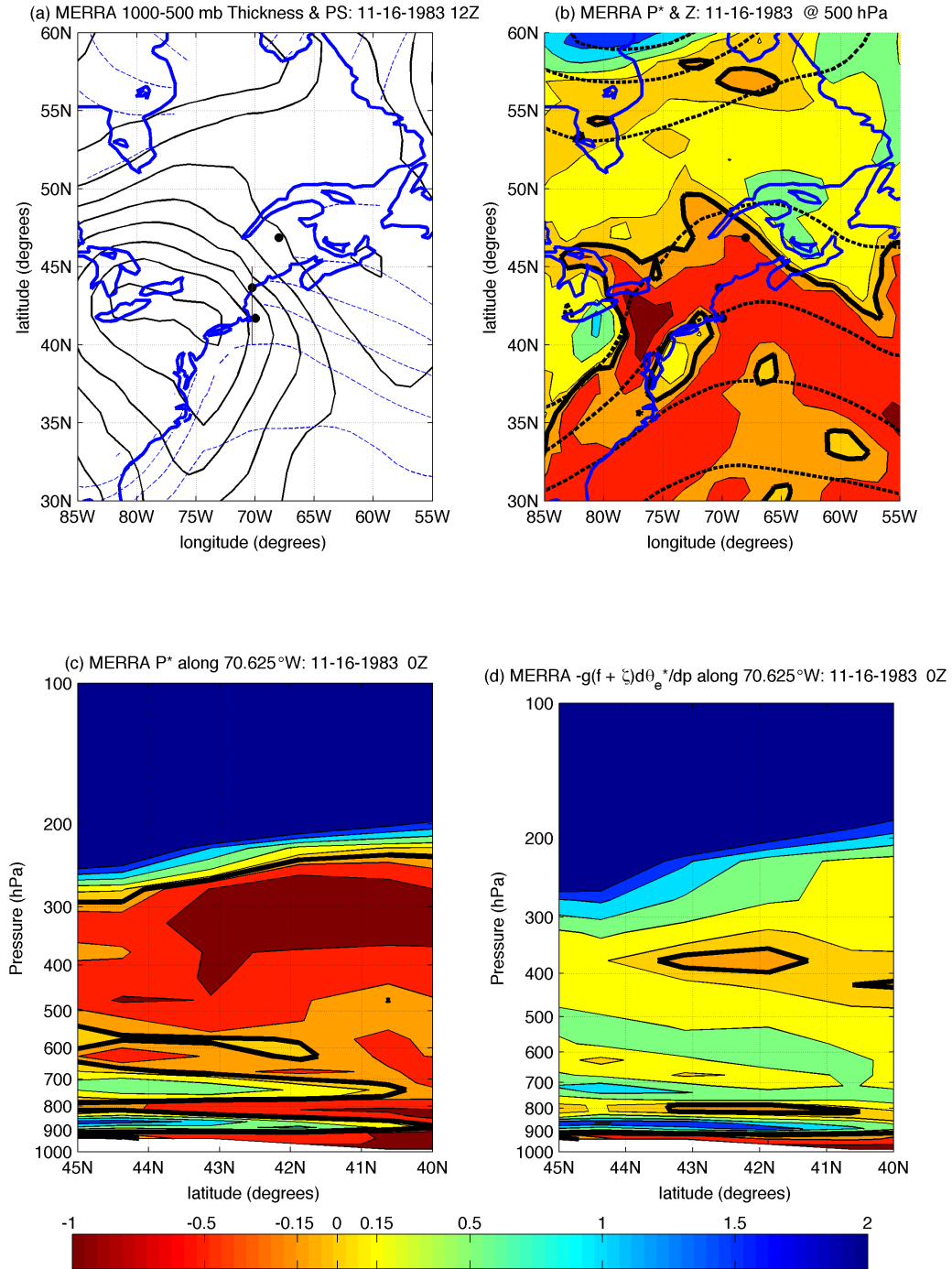


Figure 2: MERRA reanalysis for 16 November 1983 showing (a) 1000-500 mb thickness (dashed blue line), surface pressure (solid line), rawinsonde locations, cross sectional line (red line), (b) 500 hPa P^* , 500 hPa height contours (dashed line), (c) cross sectional P^* , and (d) cross sectional $-g[f + \zeta]d\theta_e^*/dp$. Values shown are in PVU.

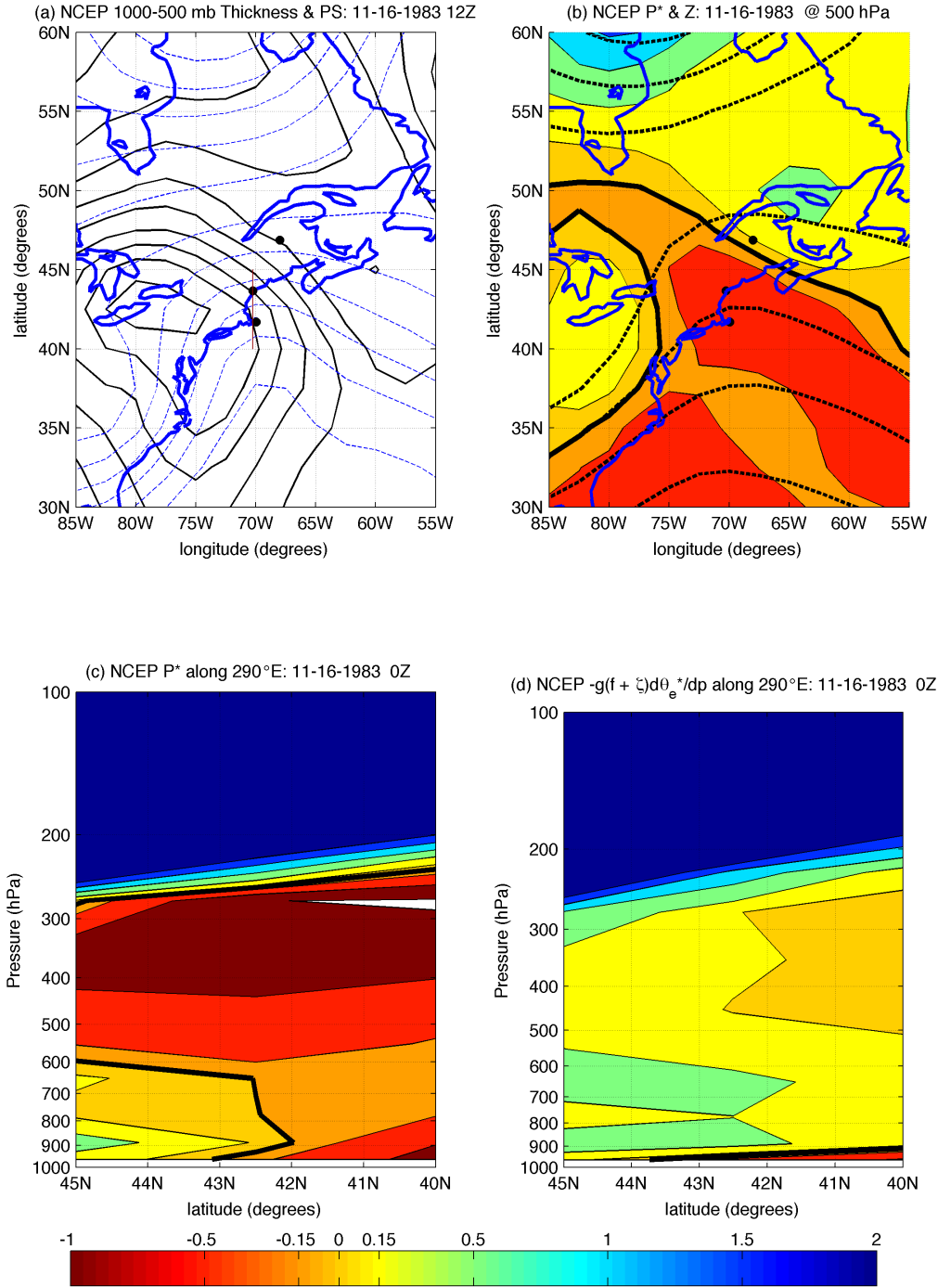


Figure 3: NCEP reanalysis for 16 November 1983 showing (a) 1000-500 mb thickness (dashed blue line), surface pressure (solid line), rawinsonde locations, cross sectional line (red line), (b) 500 hPa P^* , 500 hPa height contours (dashed line), (c) cross sectional P^* , and (d) cross sectional $-g[f + \zeta]d\theta_e^*/dp$. Values shown are in PVU.

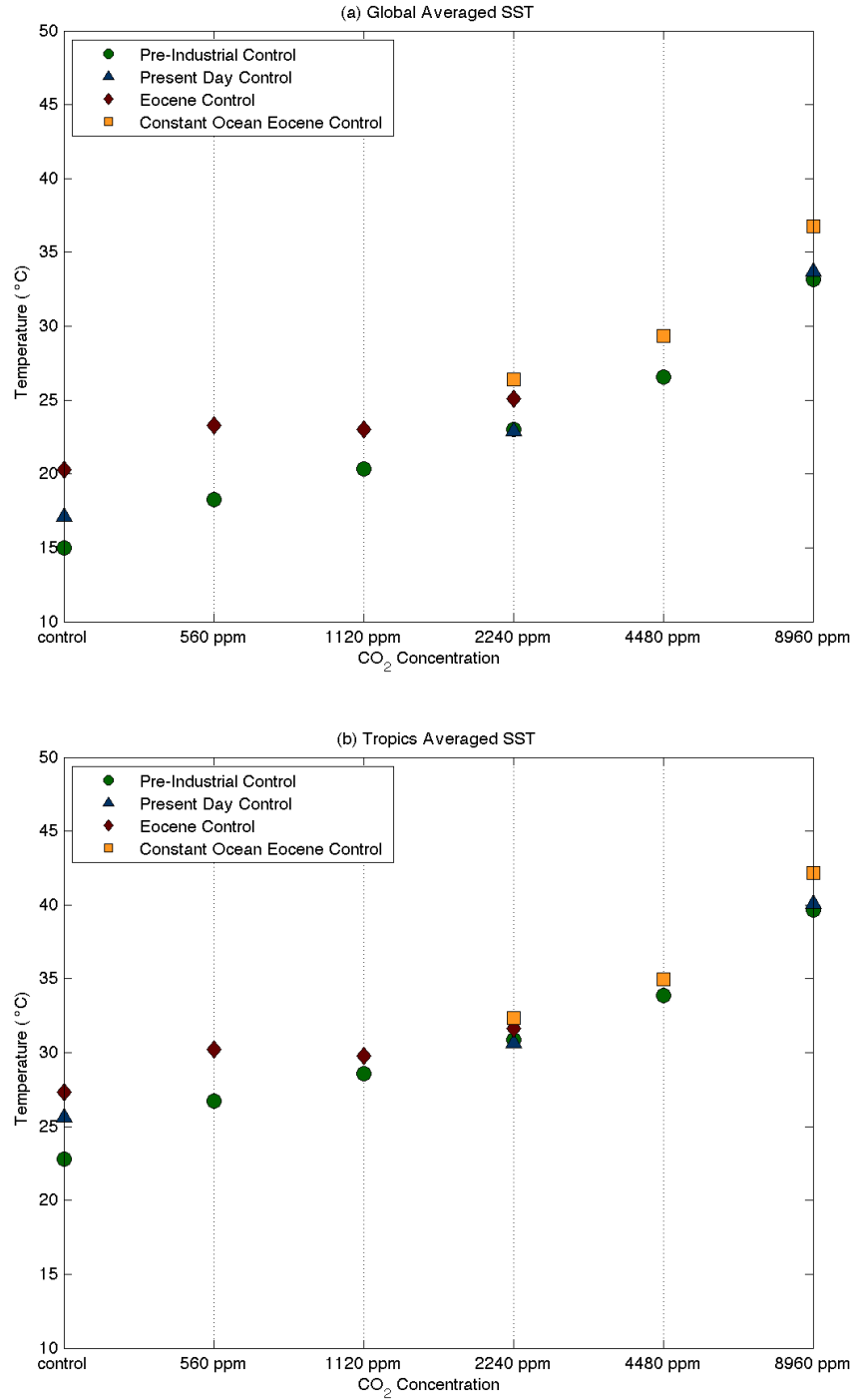


Figure 8: Climatologically averaged (a) global and (b) tropical sea surface temperatures among model simulations. Values shown are in °C.

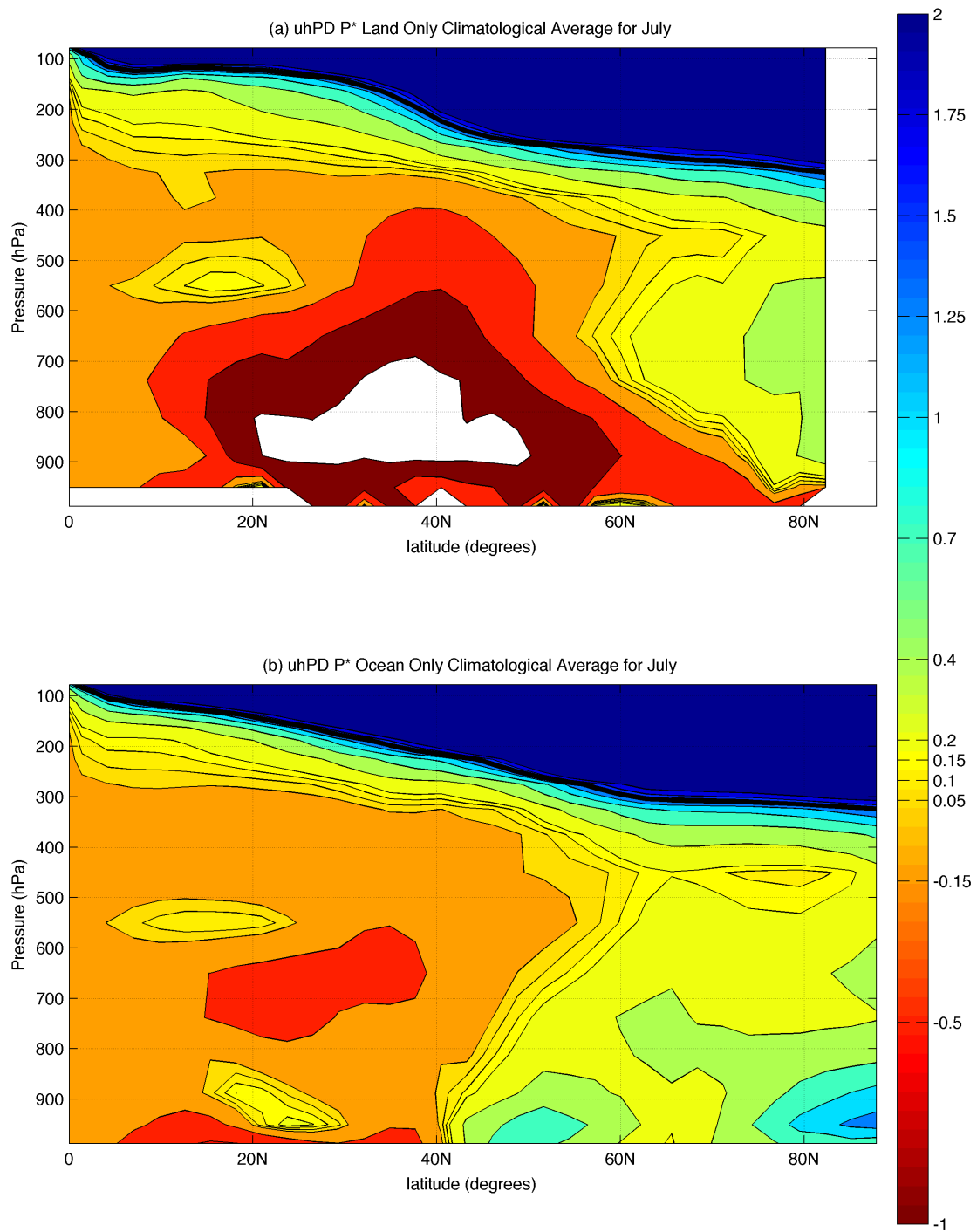


Figure 9: Control climate simulation. Climatological zonally averaged P^* over (a) land and (b) ocean in July. Values shown are in PVU (where $1 \text{ PVU} = 10^{-6} \text{ K m}^2 \text{ kg}^{-1} \text{ s}^{-1}$).

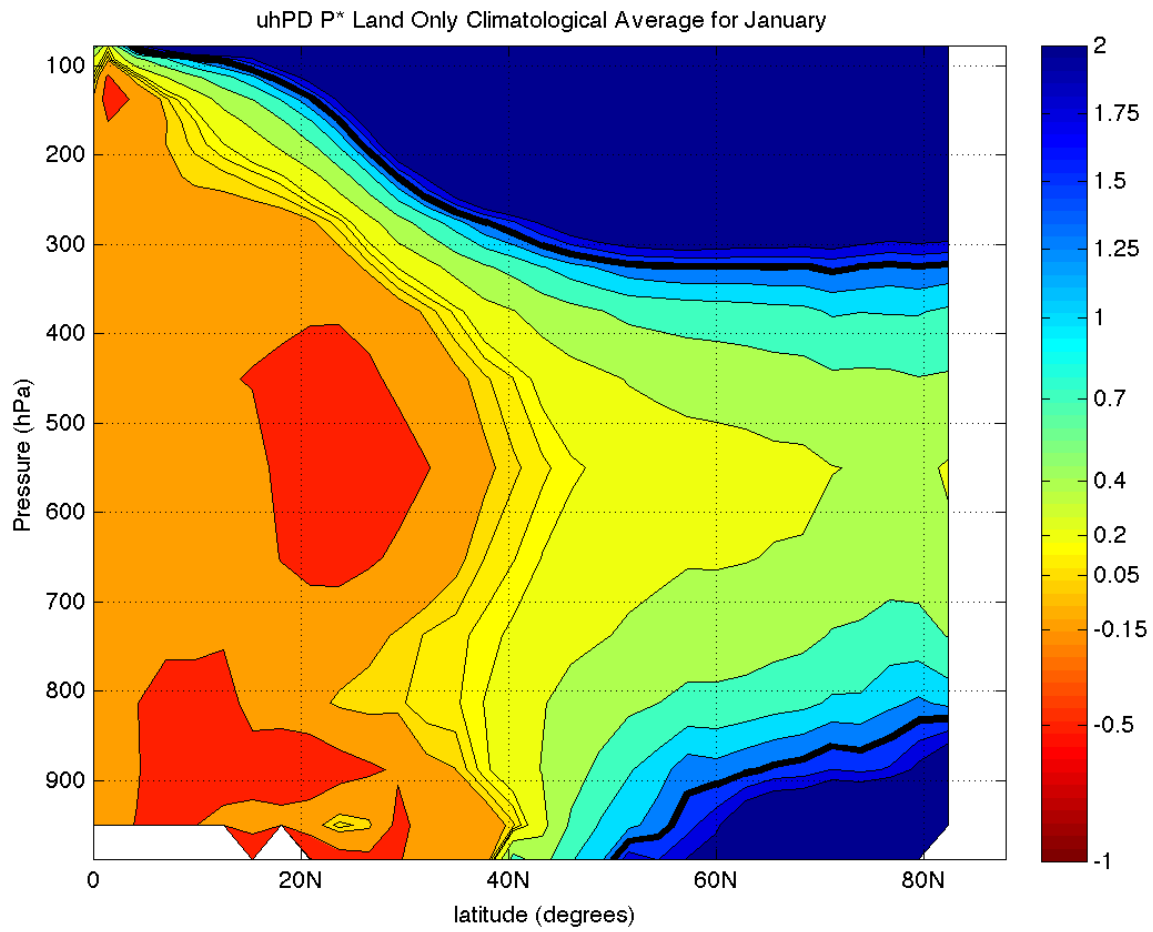


Figure 10: Control climate simulation. Climatological zonally averaged P^* over land in January. Values shown are in PVU (where $1 \text{ PVU} = 10^{-6} \text{ K m}^2 \text{ kg}^{-1} \text{ s}^{-1}$).

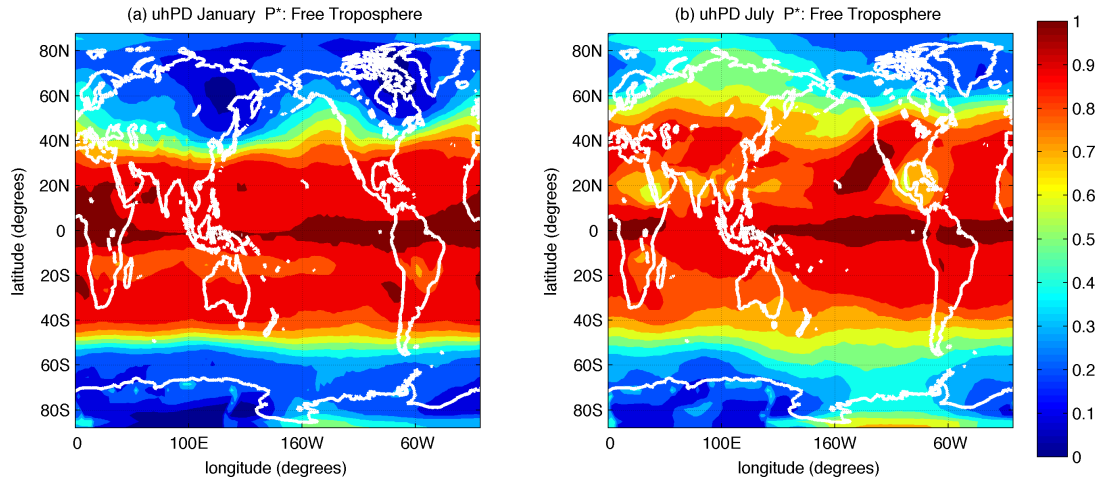


Figure 11: Control climate simulation. Climatological fraction of days for (a) January and (b) July where lapse rates are parallel or more unstable to the moist adiabatic lapse rate throughout the free troposphere (within some arbitrary threshold; in this case < 0.15 PVU).

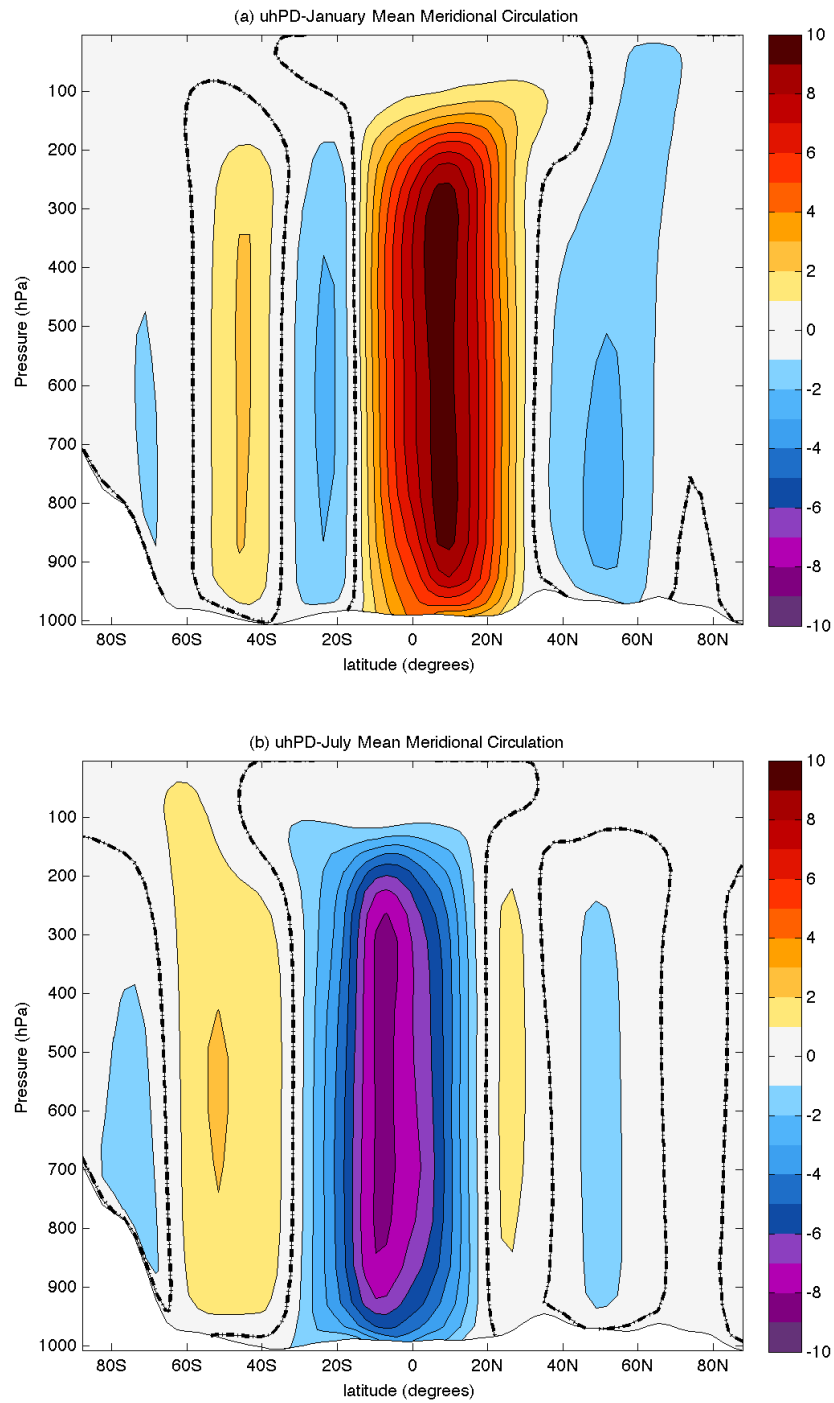


Figure 12: Control climate simulation. Climatological zonally averaged meridional circulation for (a) January and (b) July. Values shown are in m/s.

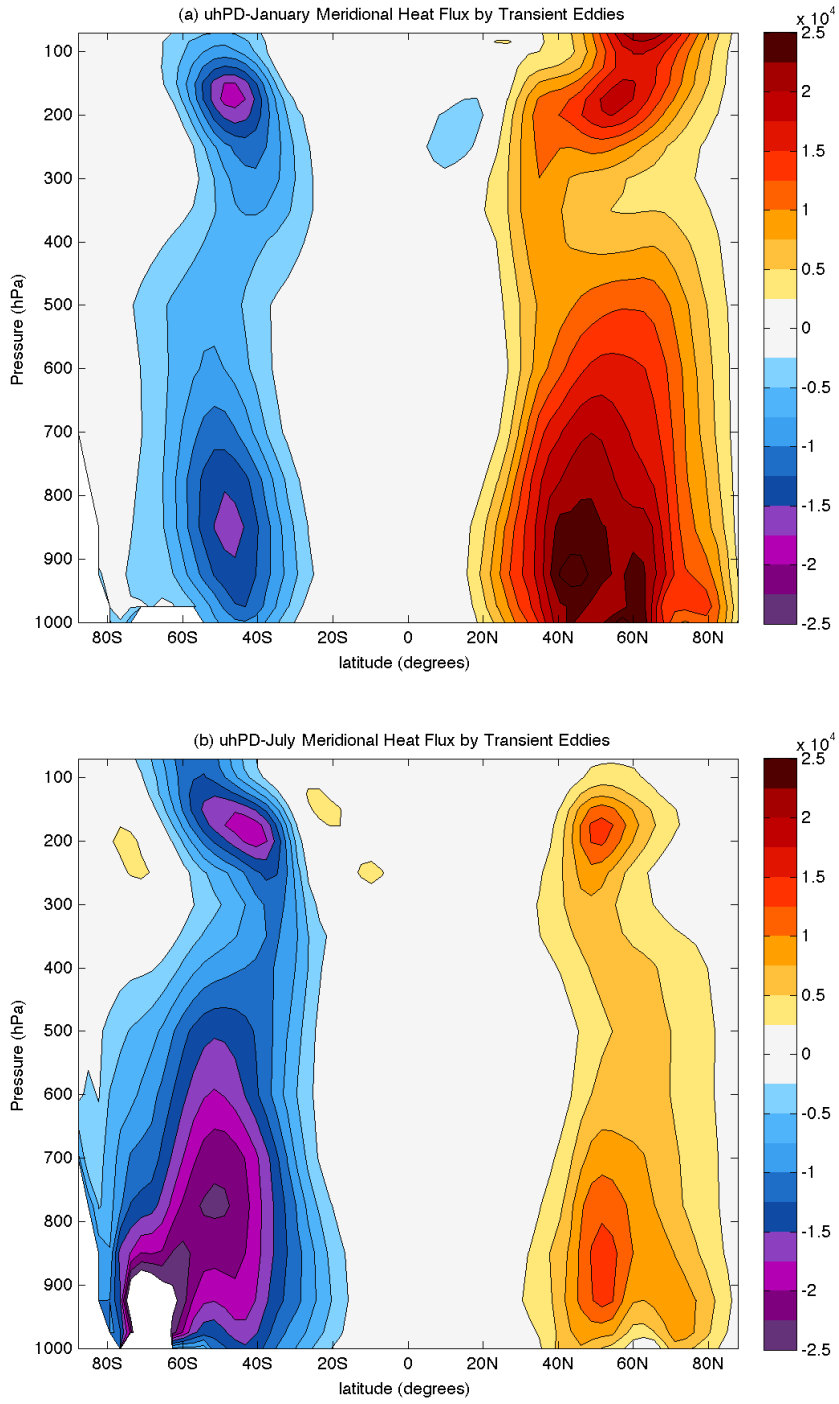


Figure 13: Control climate simulation. Climatological zonally averaged meridional heat flux by transient eddies for (a) January and (b) July. Values shown are in $\text{J kg}^{-1} \text{ m/s}$.

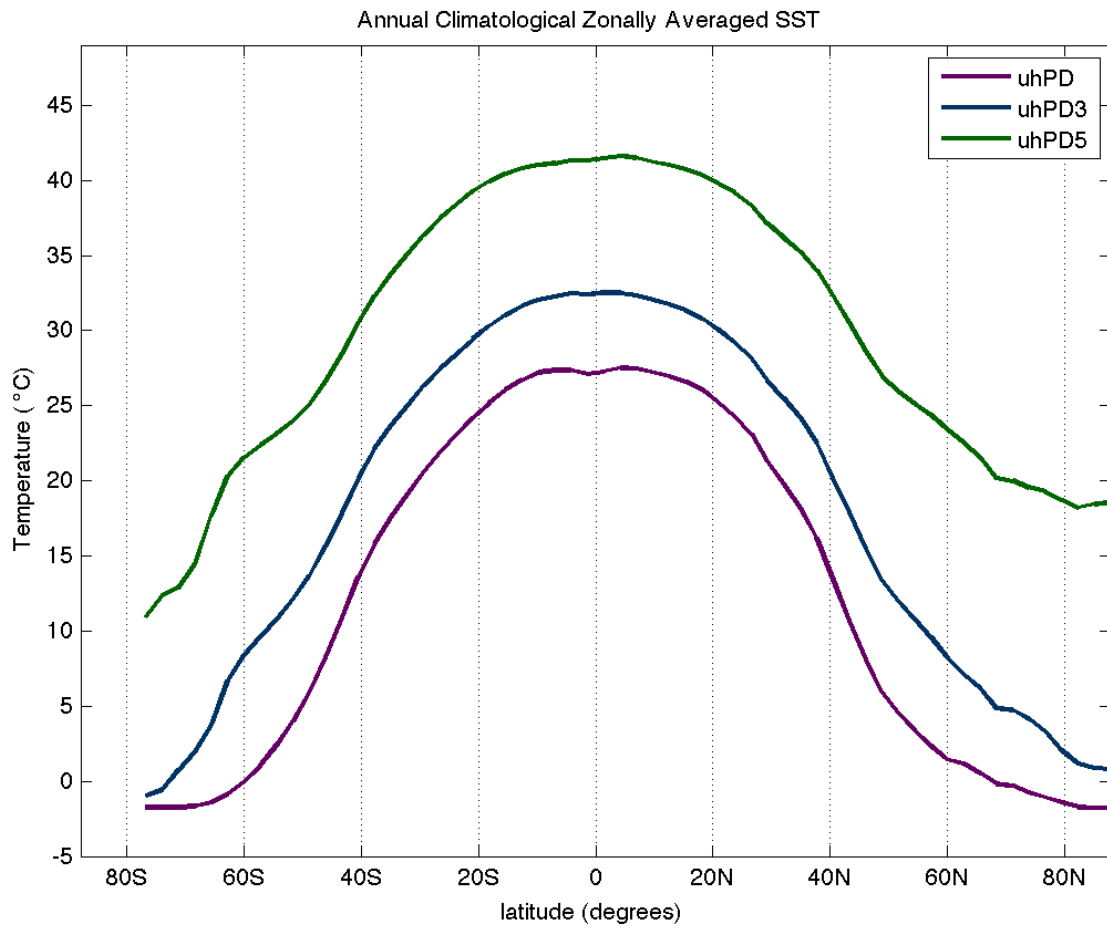


Figure 14: Annual climatological zonally averaged sea surface temperatures for control (purple), intermediate warming (blue), and exceedingly hot (green) climate simulations. Values shown are in °C.

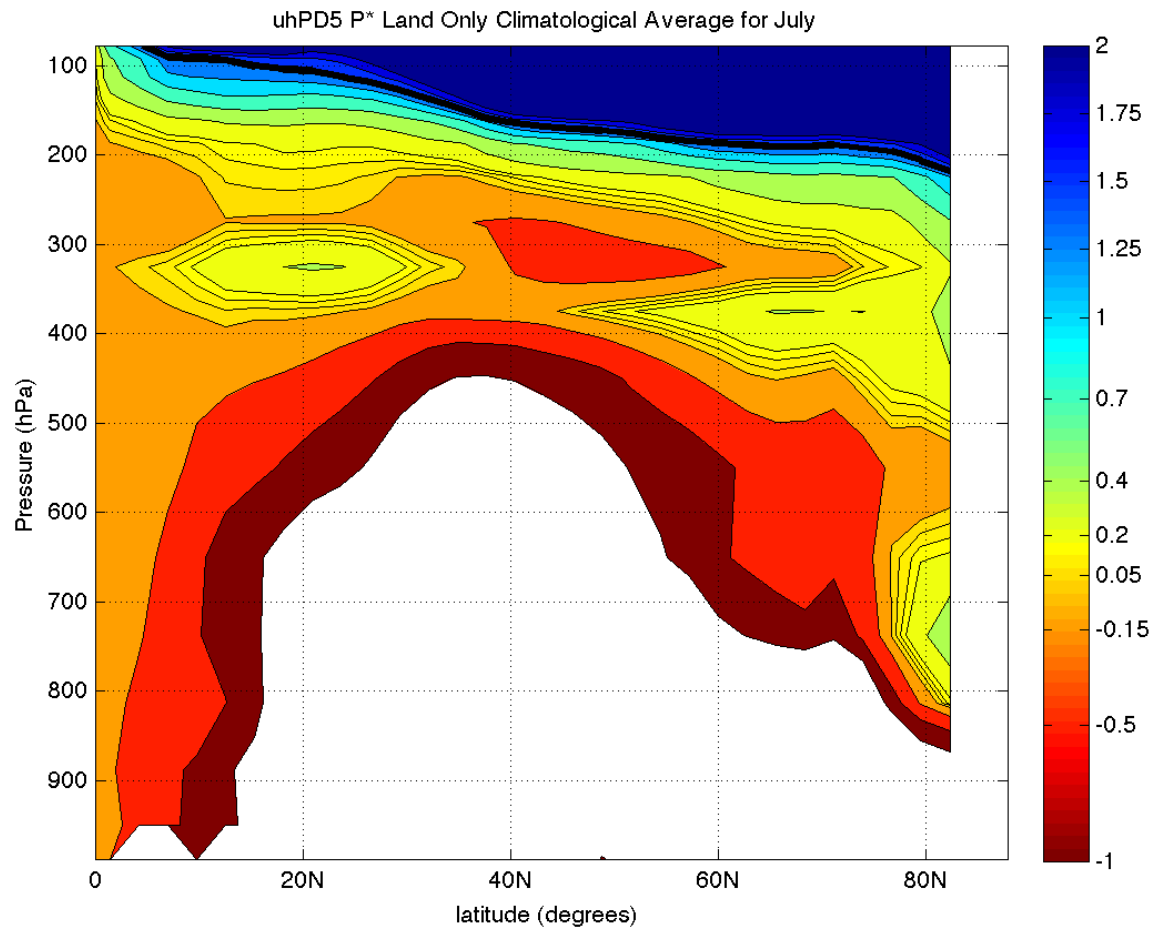


Figure 15: Exceedingly hot climate simulation. Climatological zonally averaged P^* over land in July. Values shown are in PVU (where $1 \text{ PVU} = 10^{-6} \text{ K m}^2 \text{ kg}^{-1} \text{ s}^{-1}$).

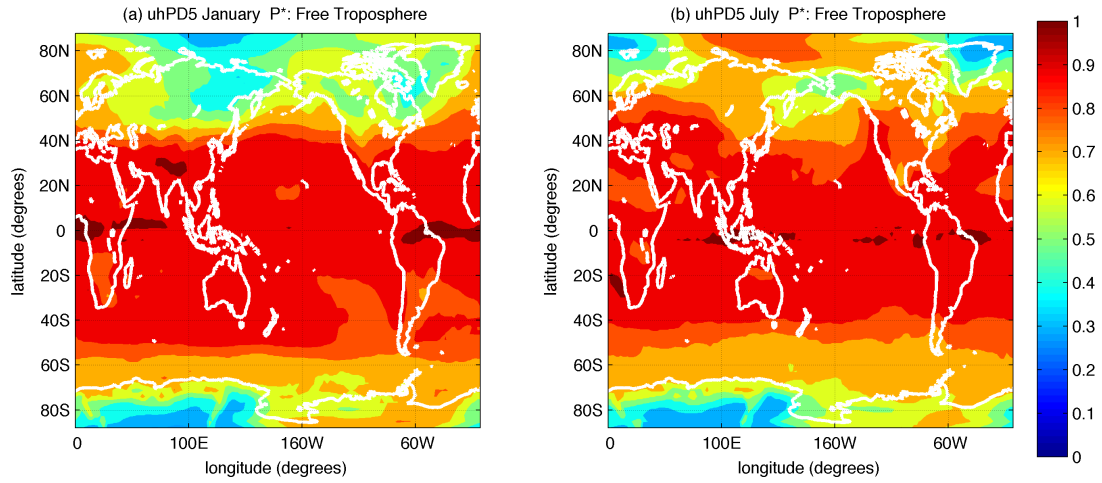


Figure 16: Exceedingly hot climate simulation. Climatological fraction of days for (a) January and (b) July where lapse rates are parallel or more unstable to the moist adiabatic lapse rate throughout the free troposphere (within some arbitrary threshold; in this case < 0.15 PVU).

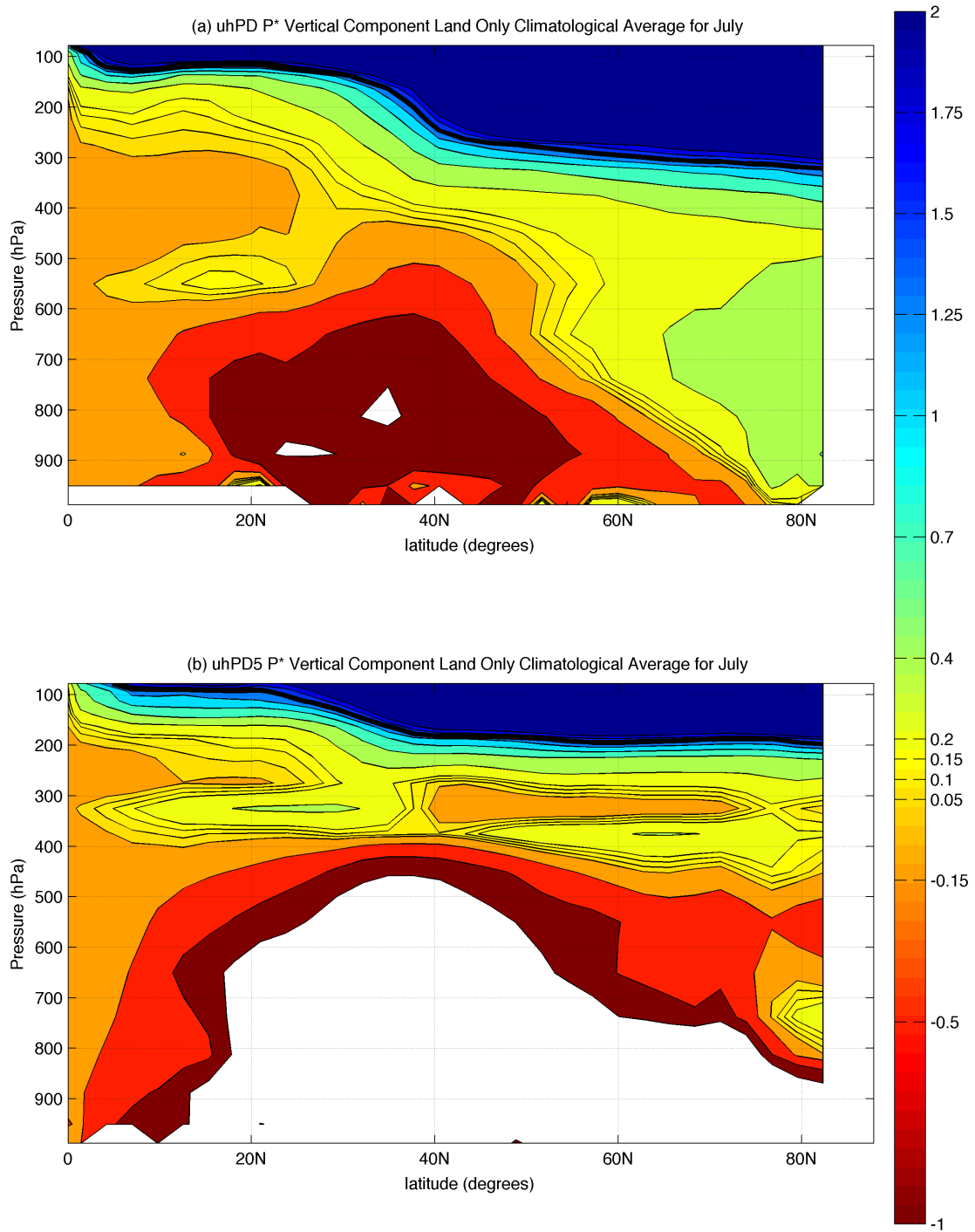


Figure 17: Climatological zonally averaged vertical component of P^* ($-g[f + \xi]d\theta_e^*/dp$) for (a) control and (b) exceedingly hot climate simulations over land in July. Values shown are in PVU.

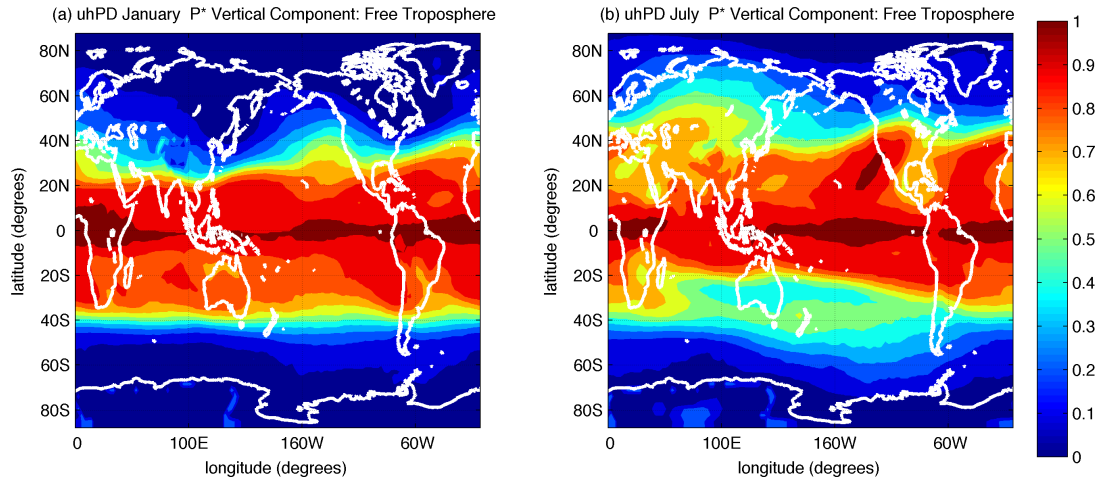


Figure 18: Control climate simulation. Climatological fraction of days for (a) January and (b) July where the vertical component of P^* ($-g[f + \zeta]d\theta_e^*/dp$) is parallel or more unstable to the moist adiabatic lapse rate throughout the free troposphere (within some arbitrary threshold; in this case < 0.15 PVU).

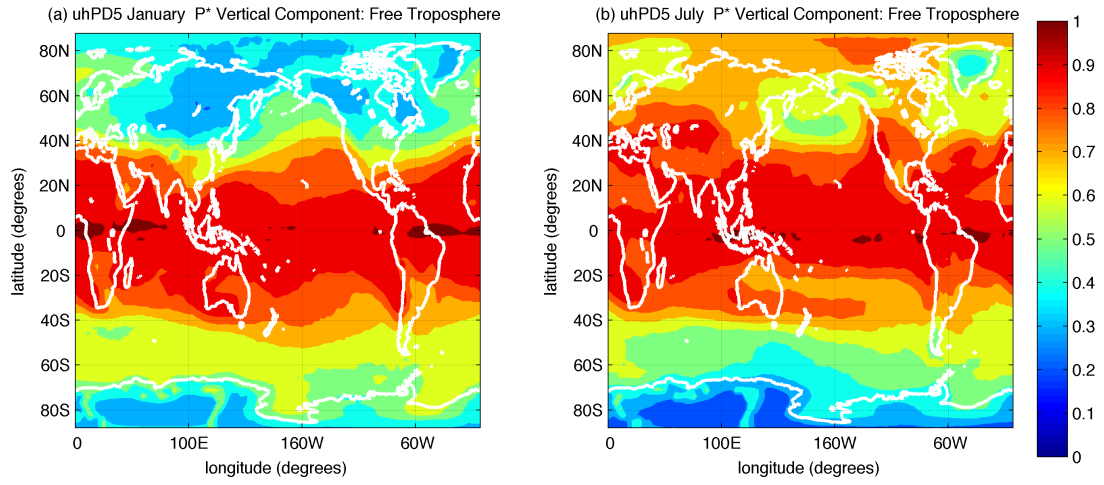


Figure 19: Exceedingly hot climate simulation. Climatological fraction of days for (a) January and (b) July where the vertical component of P^* ($-g[f+\xi]d\theta_e^*/dp$) is parallel or more unstable to the moist adiabatic lapse rate throughout the free troposphere (within some arbitrary threshold; in this case < 0.15 PVU).

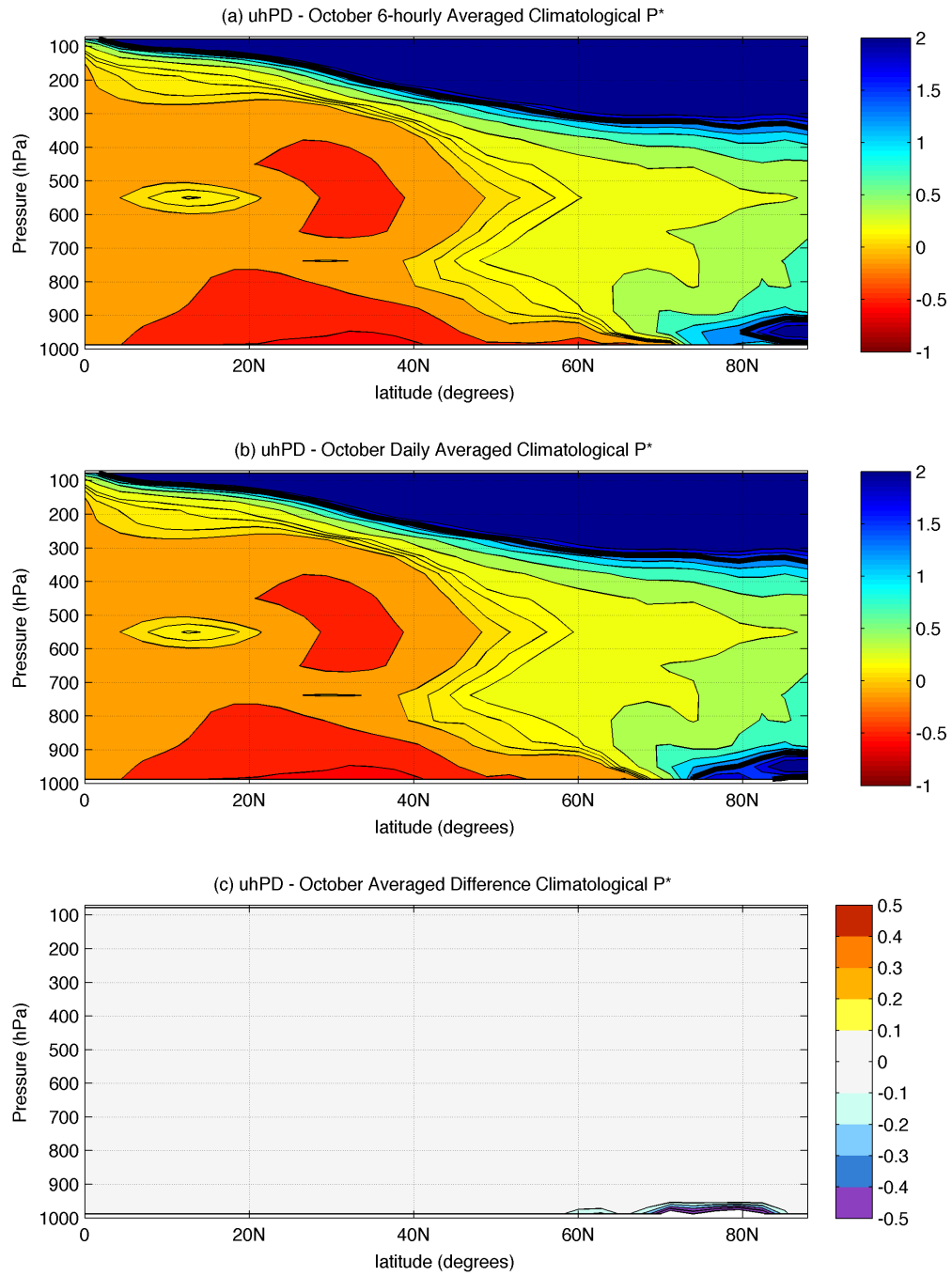


Figure 20: Control climate simulation. P^* generated for the first month of October from (a) 6-hourly averaged, (b) daily averaged, and (c) the difference between the two. Values shown are in PVU.

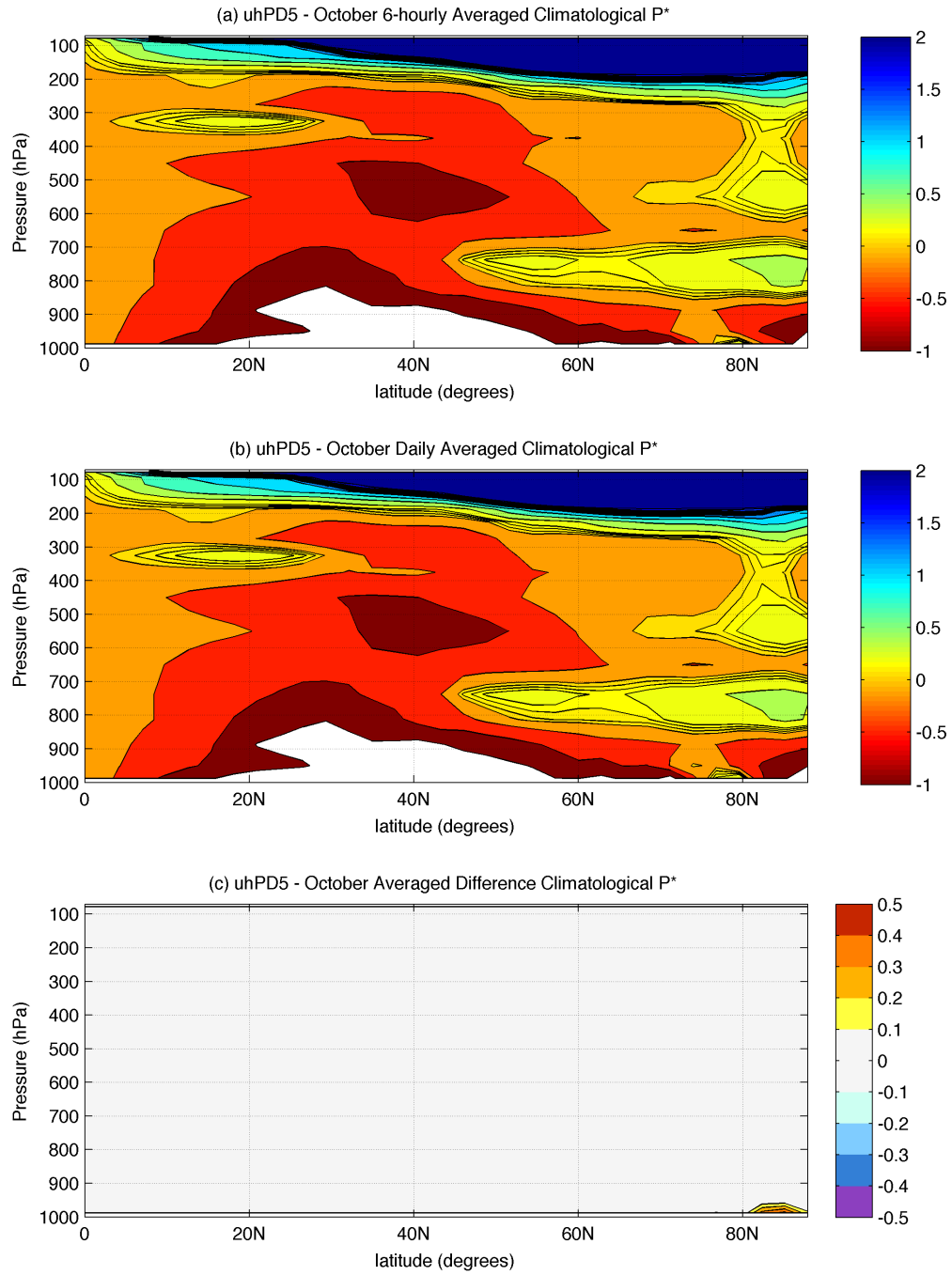


Figure 21: Exceedingly hot climate simulation. P^* generated for the first month of October from (a) 6-hourly, (b) daily averaged, and (c) the difference between the two.

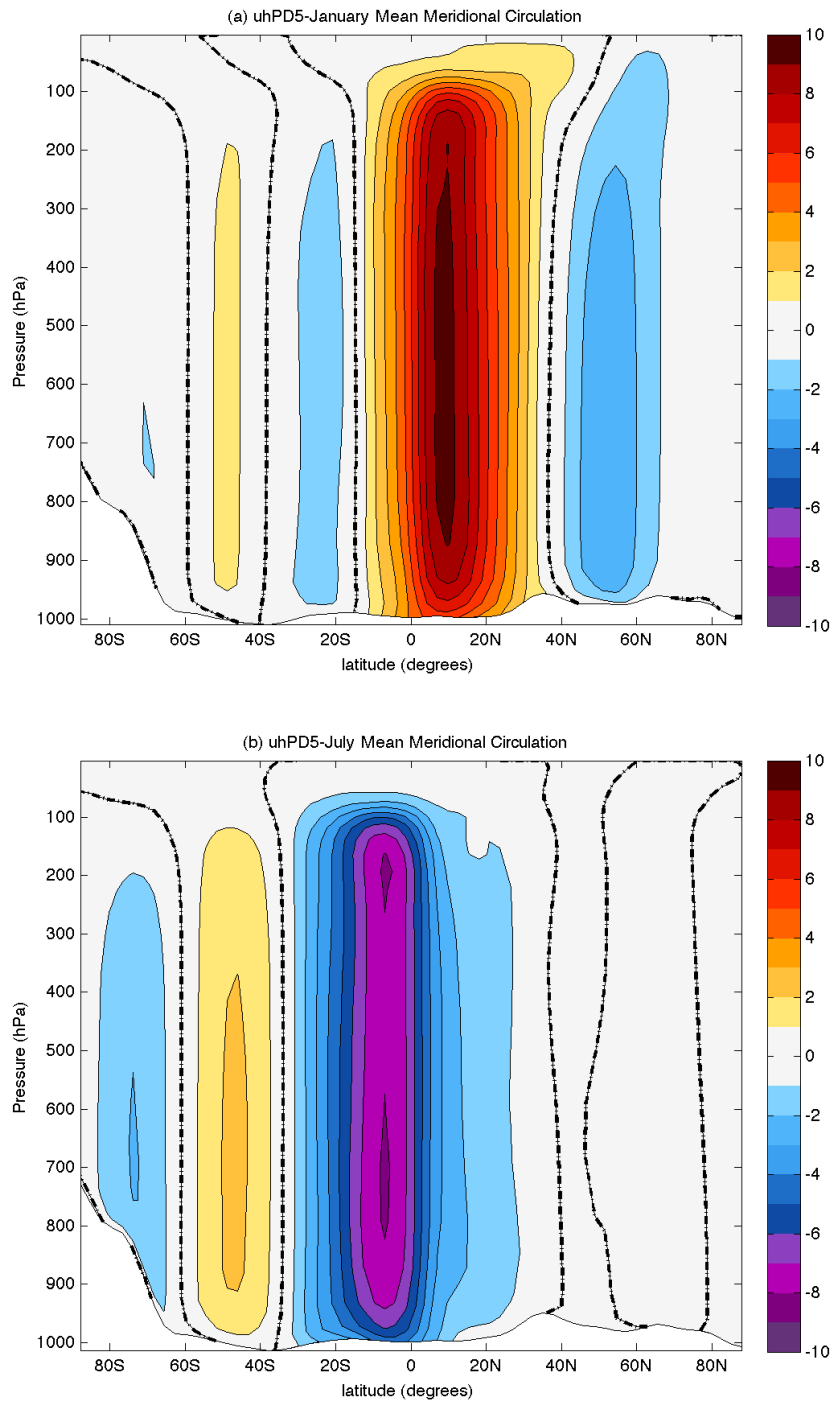


Figure 22: Exceedingly hot climate simulation. Climatological zonally averaged meridional circulation for (a) January and (b) July. Values shown are in m/s.

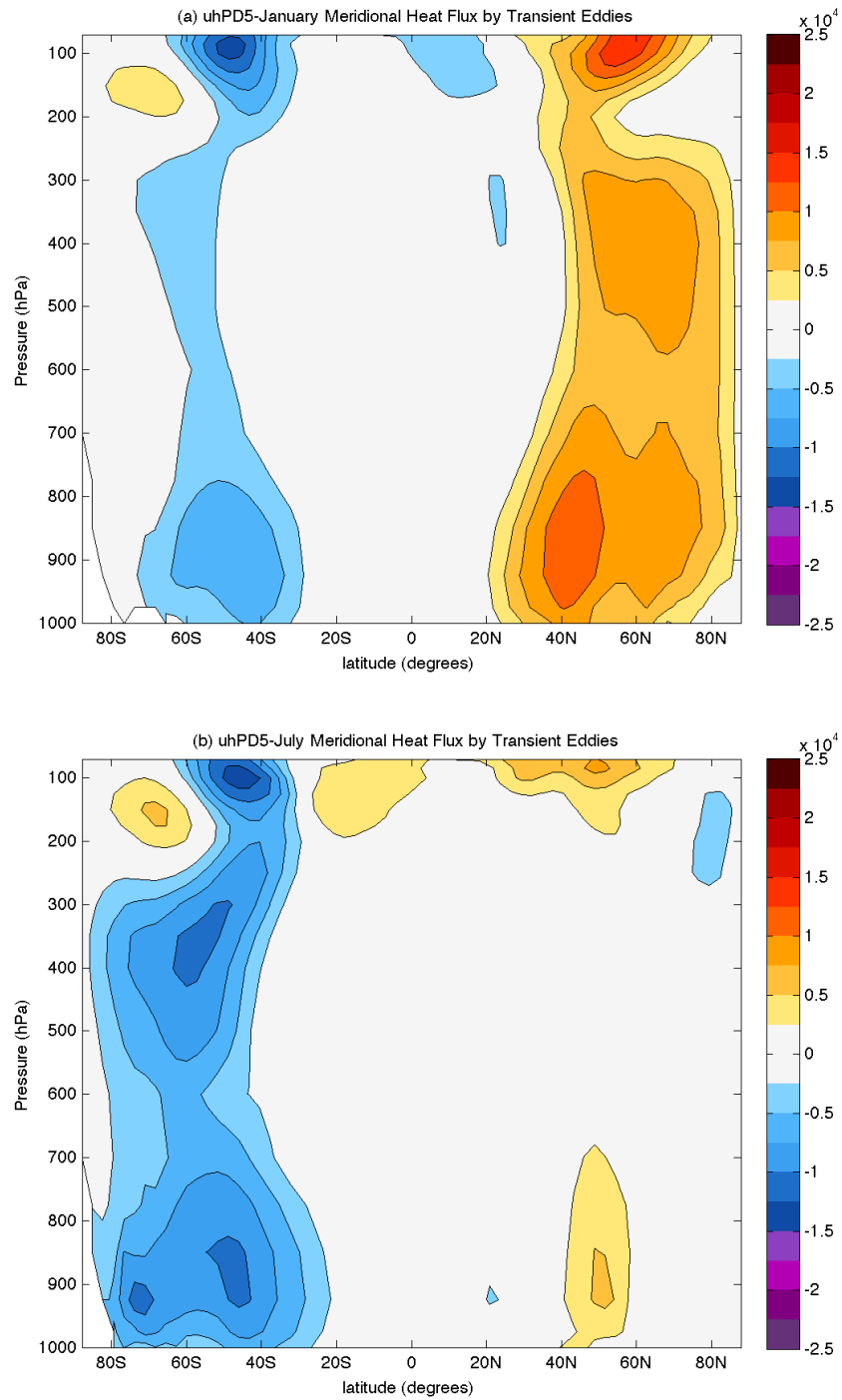


Figure 23: Exceedingly hot climate simulation. Climatological zonally averaged meridional heat flux by transient eddies for (a) January and (b) July. Values shown are in $\text{J kg}^{-1} \text{ m/s}$.

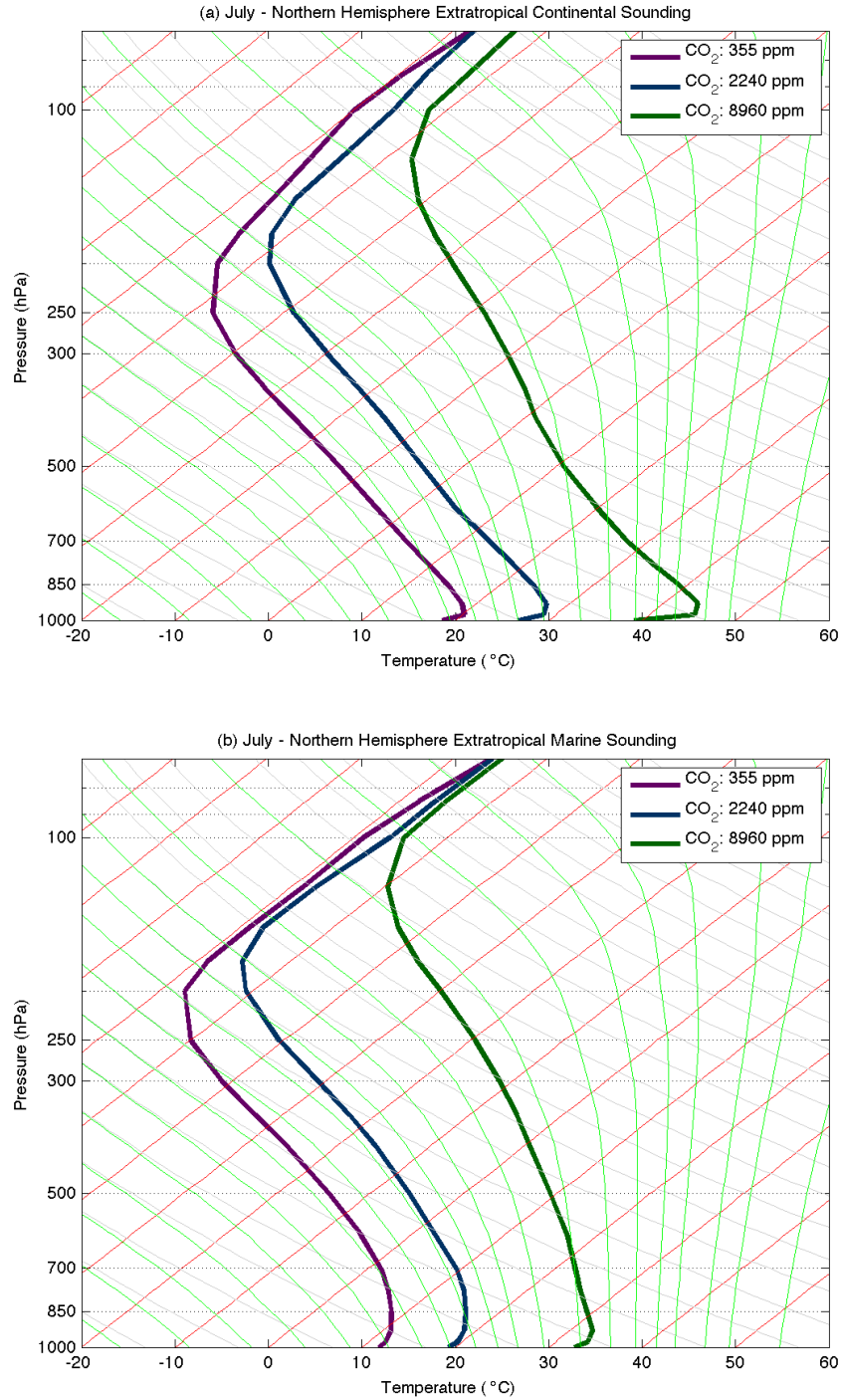


Figure 24: Climatologically averaged Extratropical sounding over (a) land and (b) ocean for control (purple), intermediate warming (blue), and exceedingly hot (green) climate simulations. Values shown are in °C.

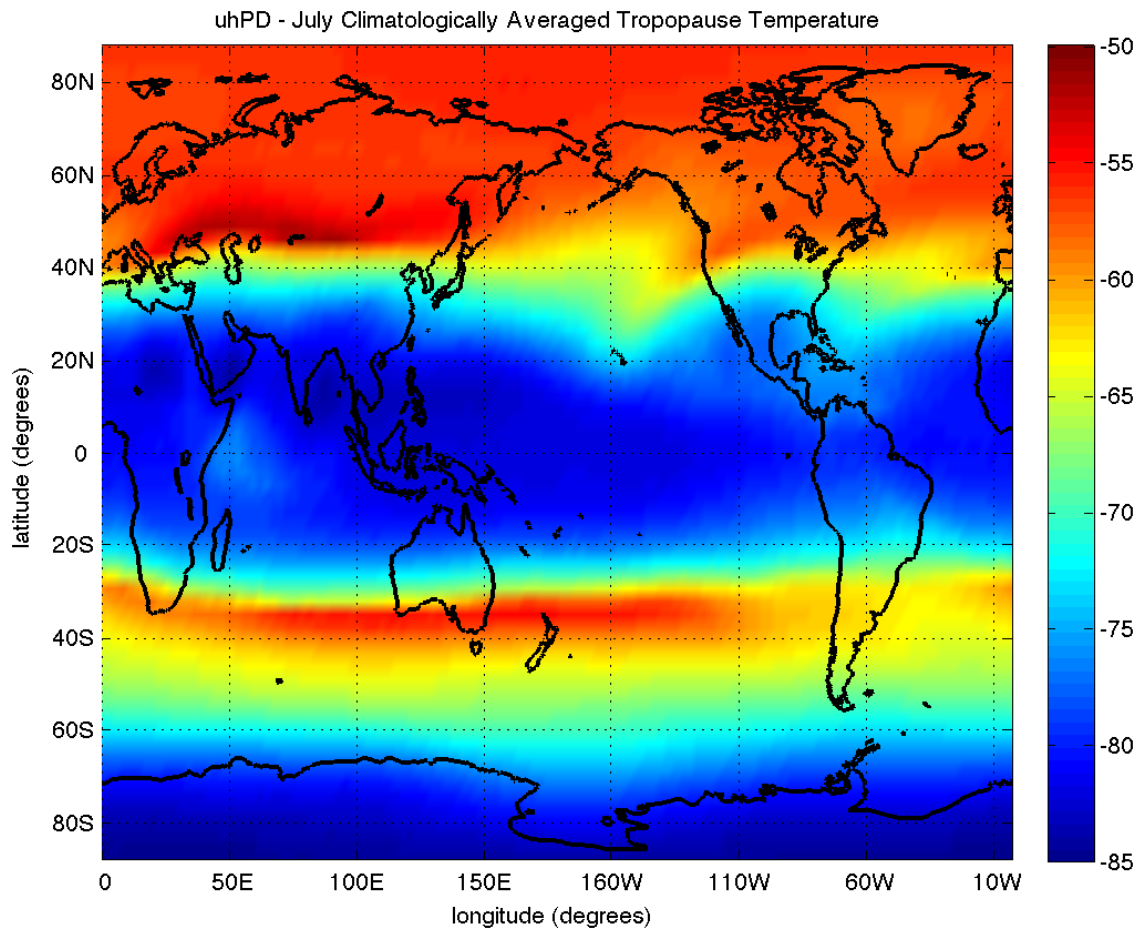


Figure 25: Control climate simulation. Climatologically averaged tropopause temperature for July. Values shown are in °C.

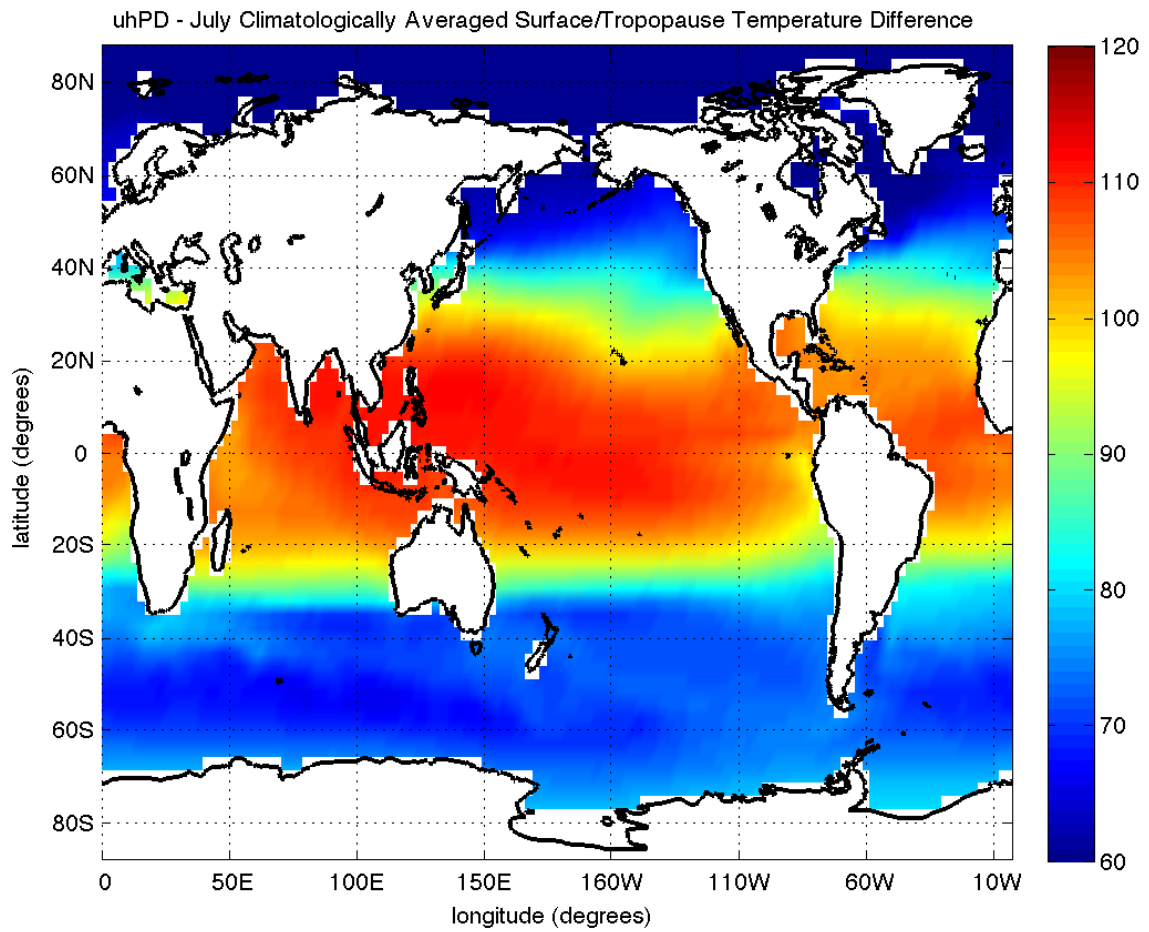


Figure 26: Control climate simulation. Climatologically averaged temperature difference between the sea surface and tropopause. Values shown are in °C.

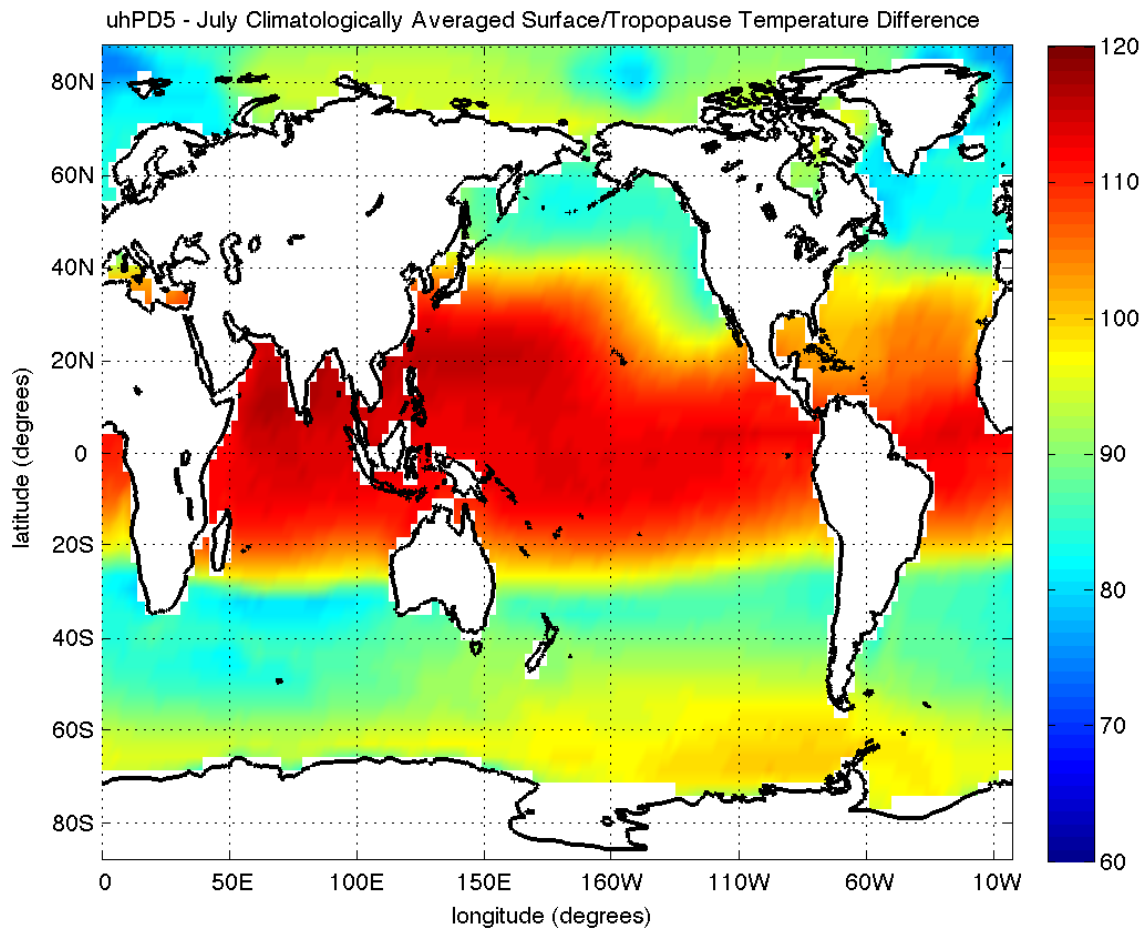


Figure 27: Exceedingly hot climate simulation. Climatologically averaged temperature difference between the sea surface and tropopause. Values shown are in °C.

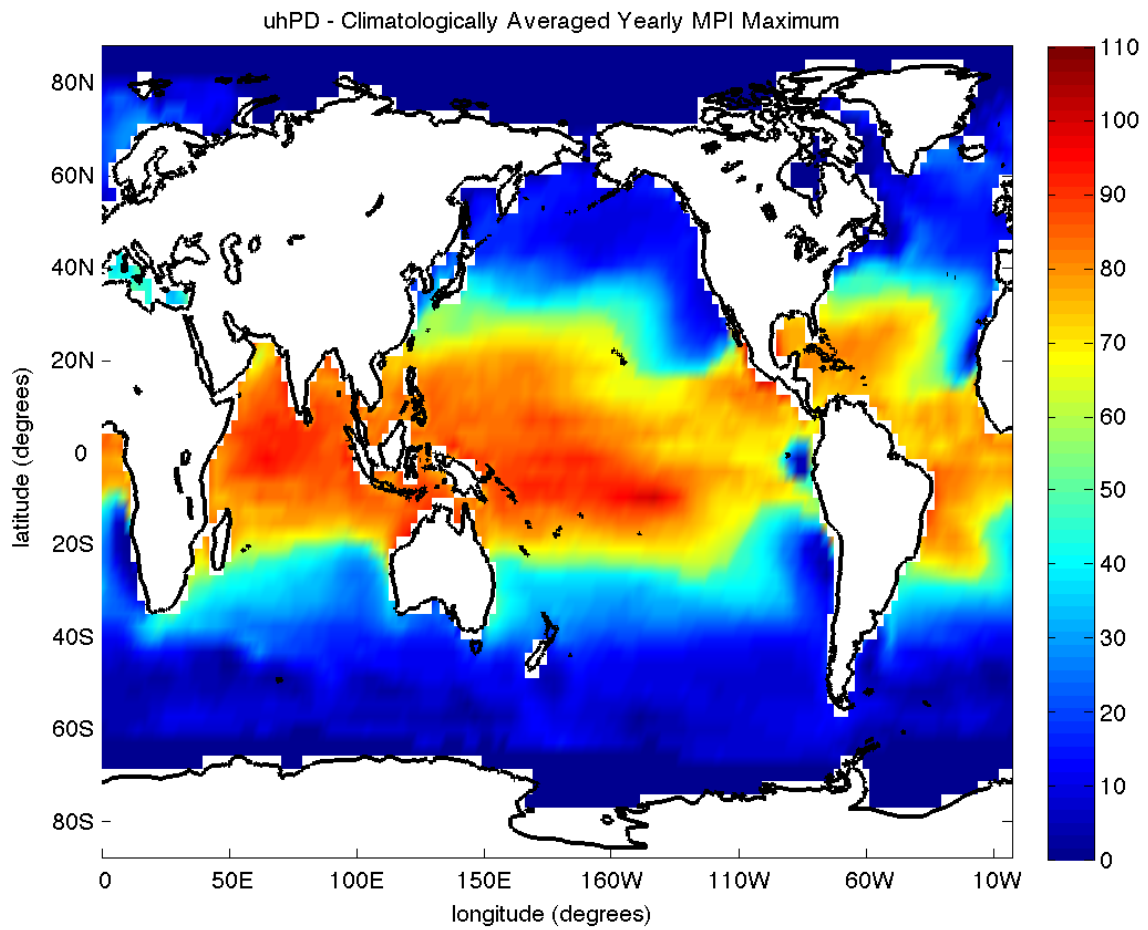


Figure 28: Control climate simulation. Maximum monthly averaged Maximum Potential Intensity (MPI). Values shown are in m/s.

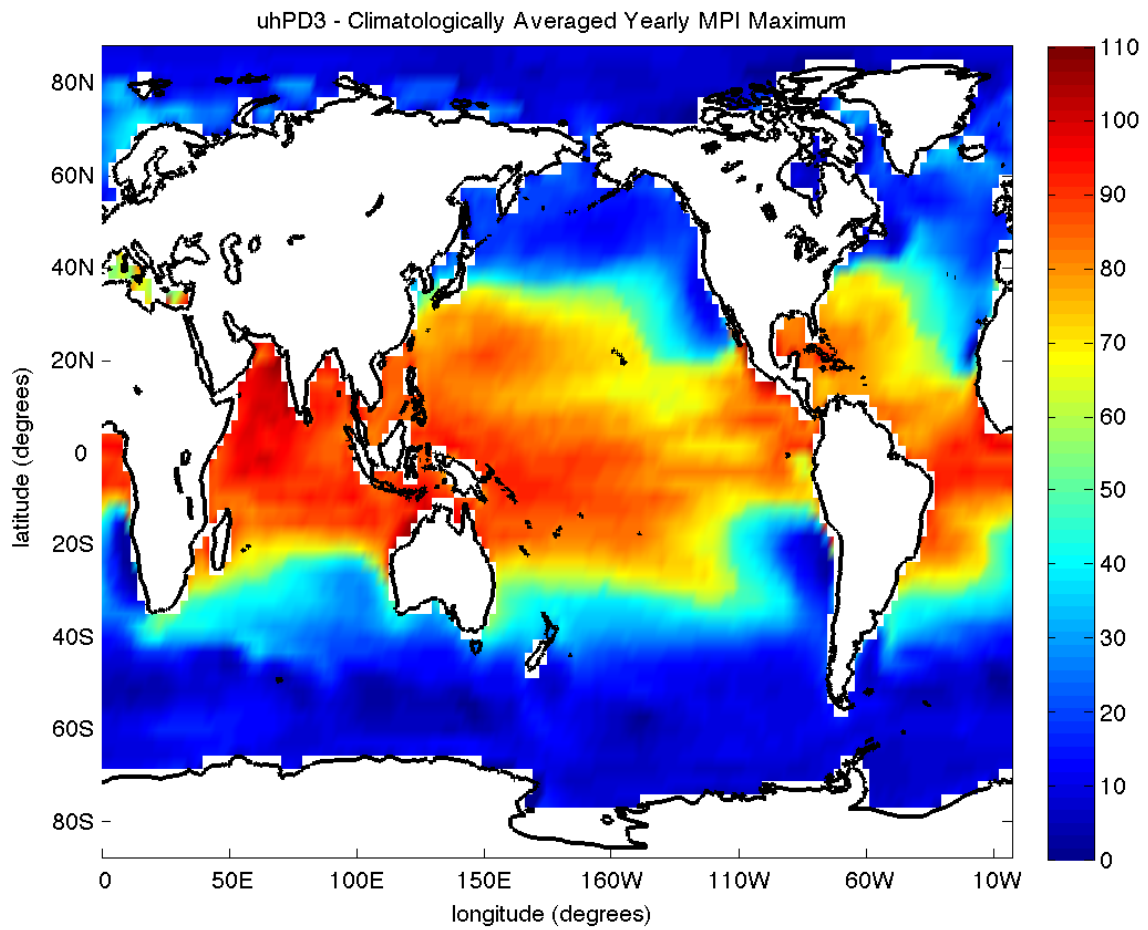


Figure 29: Intermediate warming climate simulation. Maximum monthly averaged Maximum Potential Intensity (MPI). Values shown are in m/s.

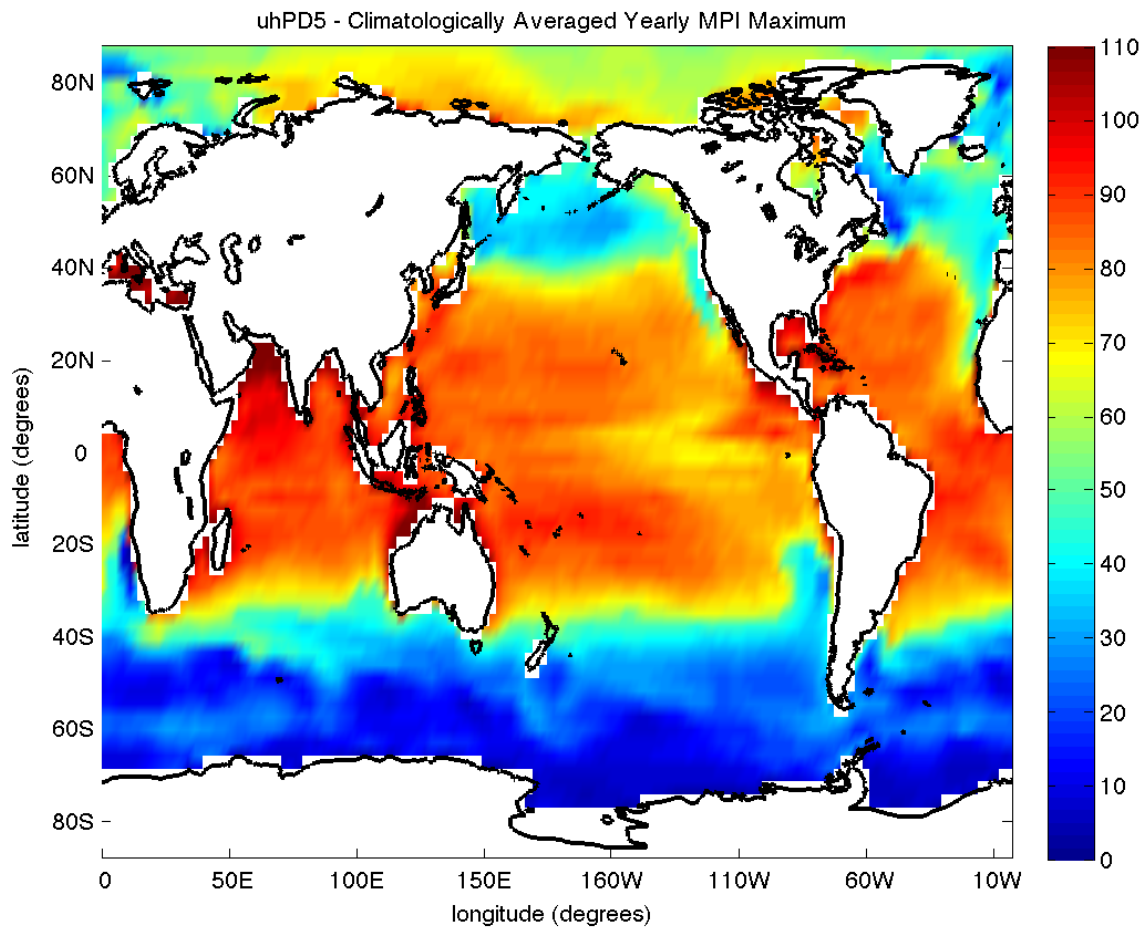


Figure 30: Exceedingly hot climate simulation. Maximum monthly averaged Maximum Potential Intensity (MPI). Values shown are in m/s.

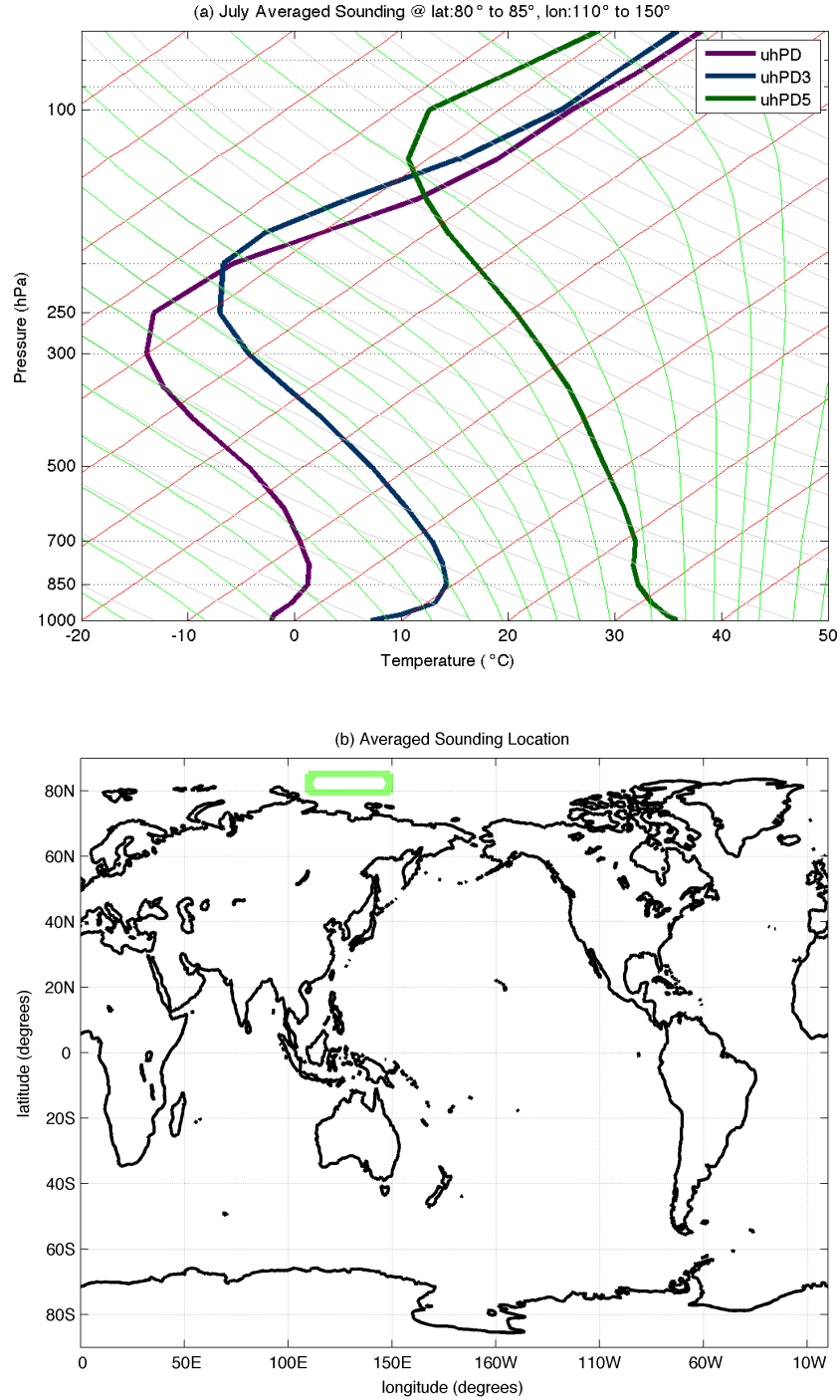


Figure 31: Climatologically averaged (a) sounding for the control (purple), intermediate warming (blue), and exceedingly hot (green) climate simulations over the region shown in (b). Values shown are in °C.

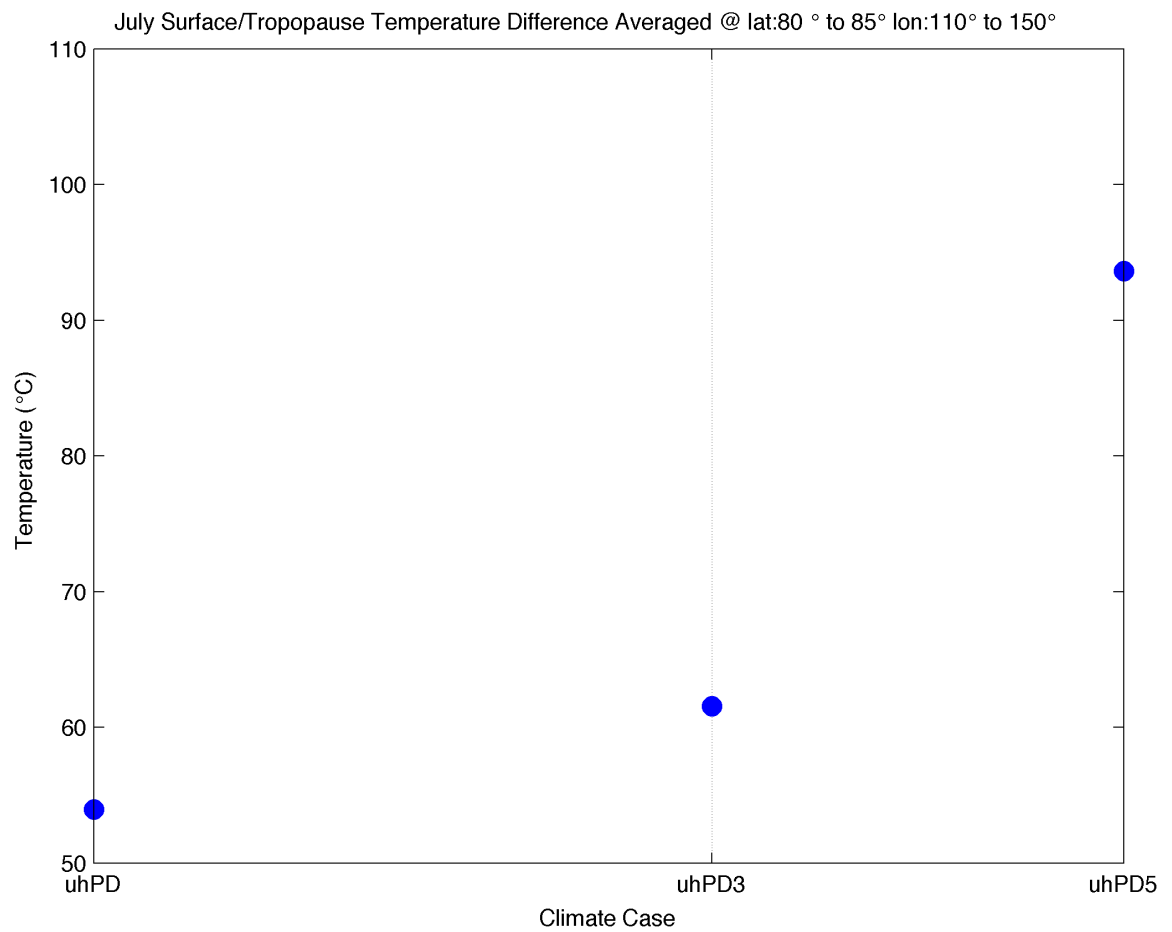


Figure 32: Climatologically averaged temperature difference between sea surface and tropopause over the region shown in Figure 31b for the control, intermediate warming, and exceedingly hot climate simulations. Values shown are in °C.

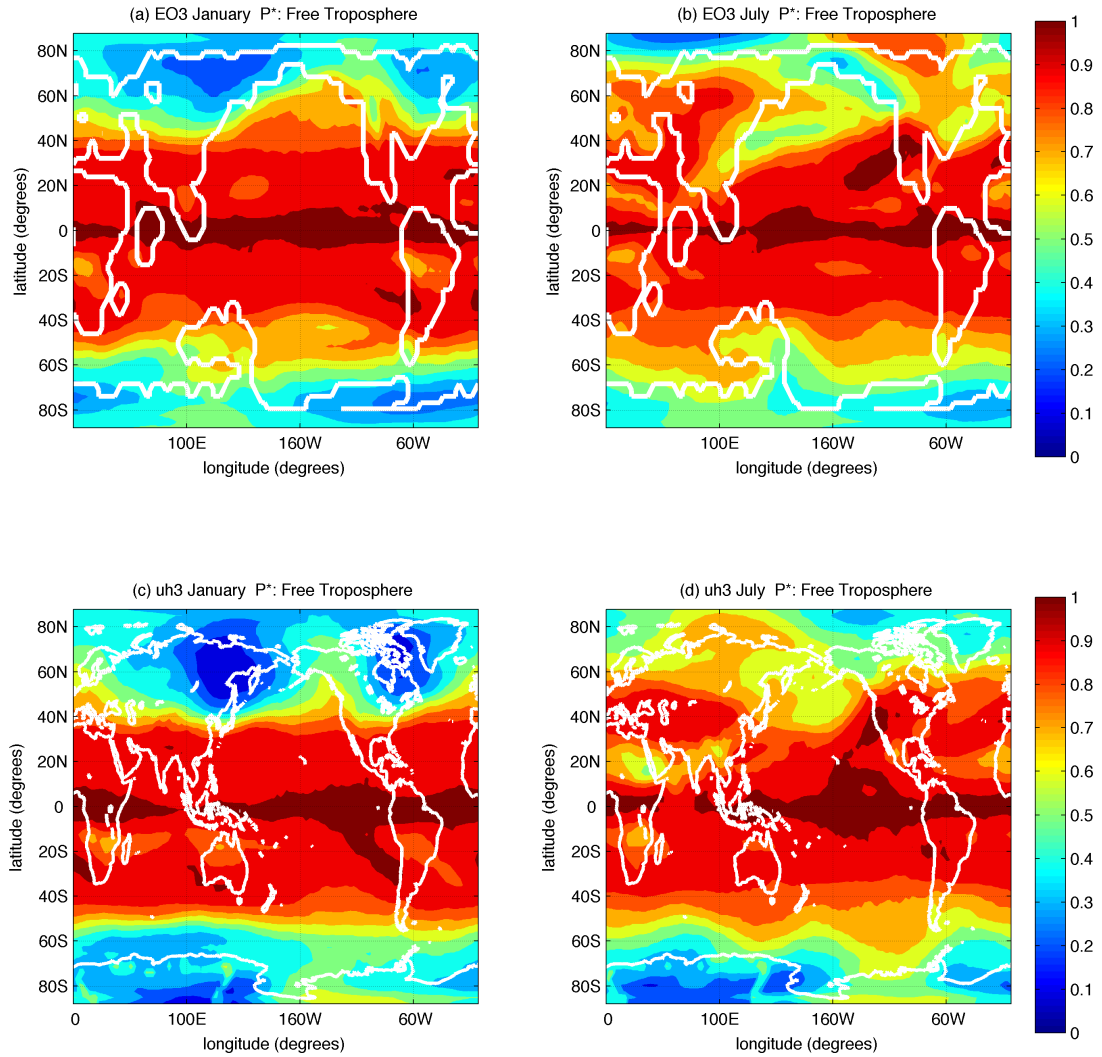


Figure 33: Intermediate warming climate simulation. Eocene scheme climatological fraction of days for (a) January and (b) July where lapse rates are parallel or more unstable to the moist adiabatic lapse rate throughout the free troposphere (within some arbitrary threshold; in this case < 0.15 PVU). Repeated for (c) and (d) for pre-industrial simulations.

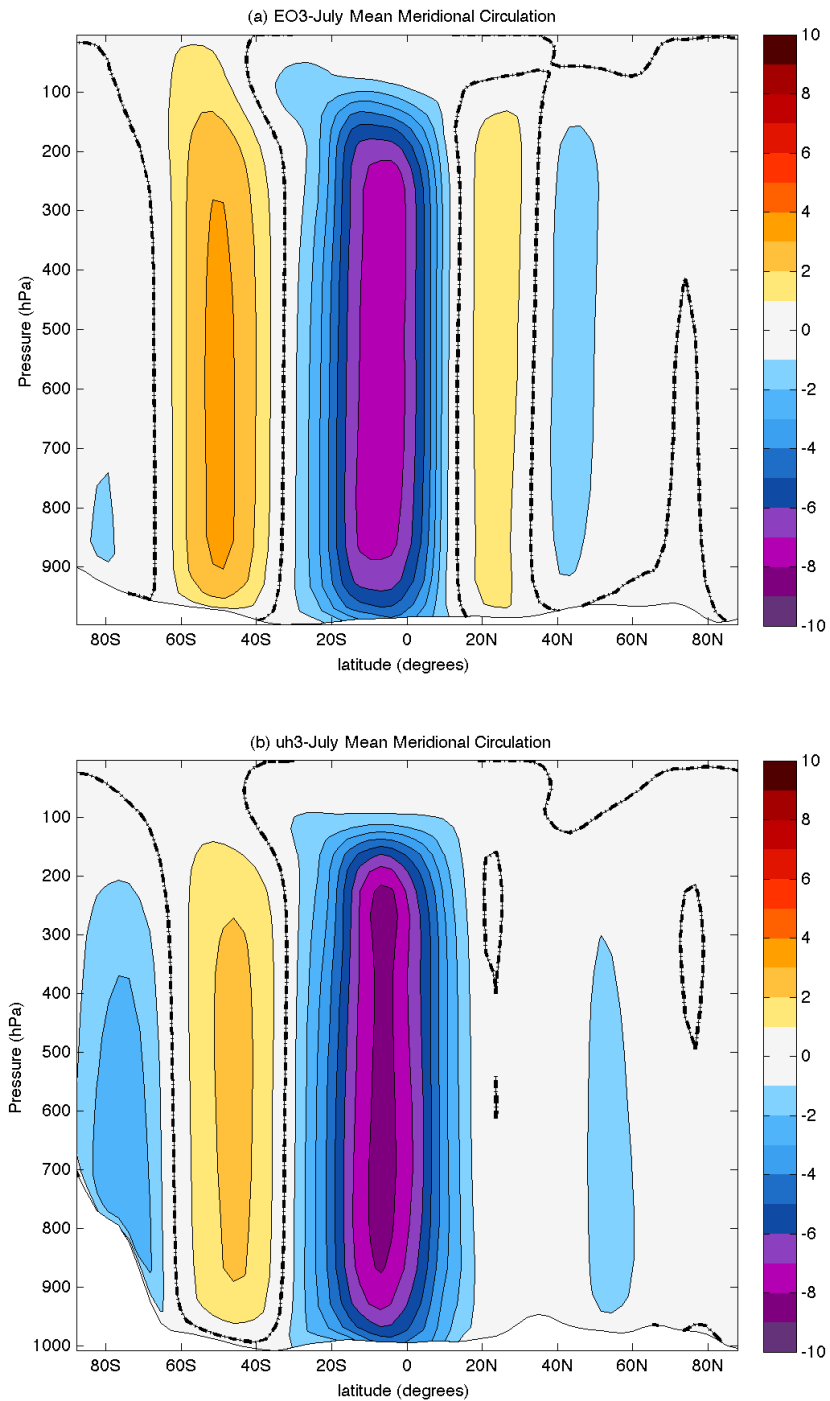


Figure 34: Intermediate warming climate simulation. Climatological zonally averaged meridional circulation during July for (a) Eocene and (b) pre-industrial schemes. Values shown are in m/s.

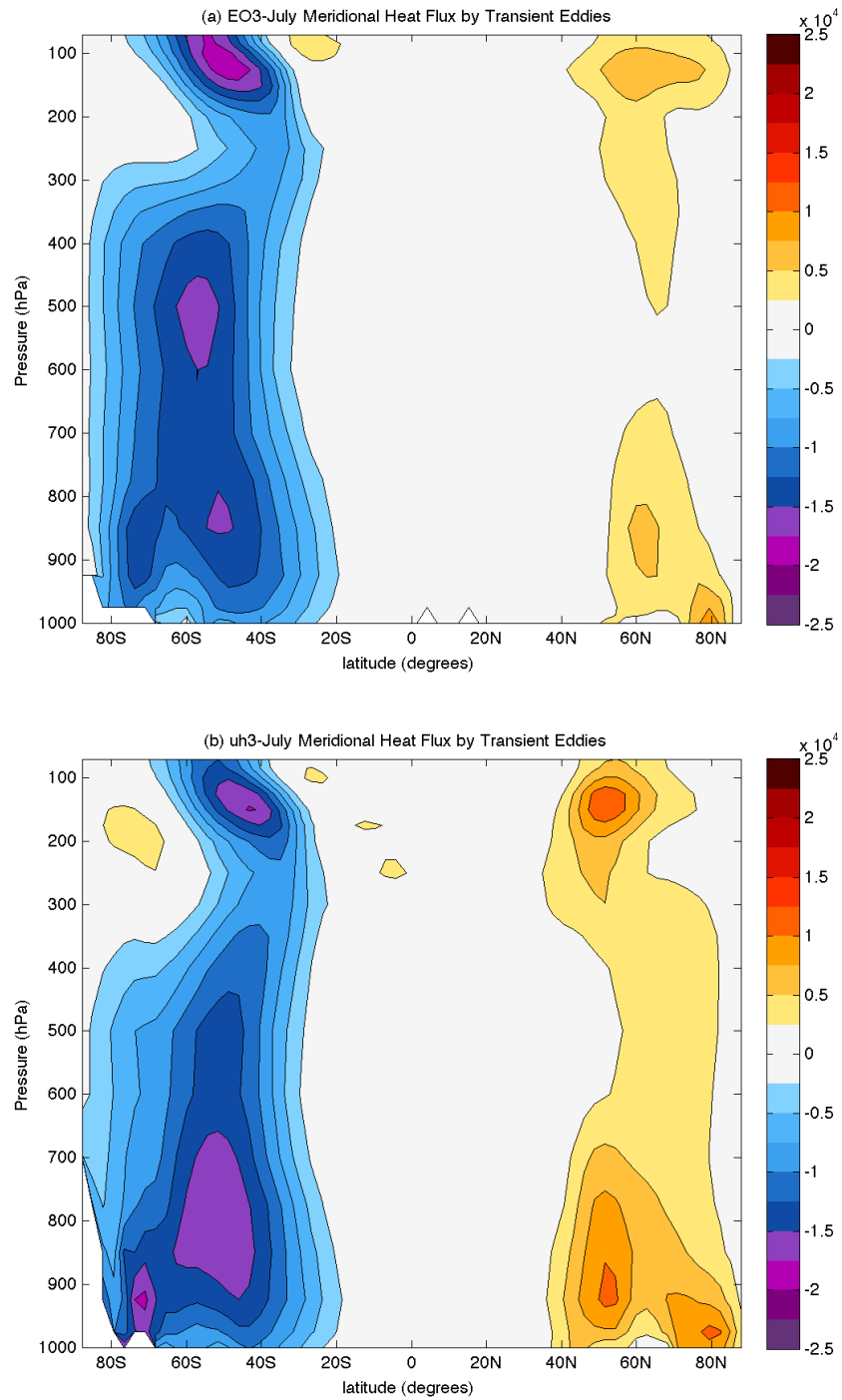


Figure 35: Intermediate warming climate simulation. Climatological zonally averaged meridional heat flux by transient eddies during July for (a) Eocene and (b) pre-industrial schemes. Values shown are in $\text{J kg}^{-1} \text{ m/s}$.

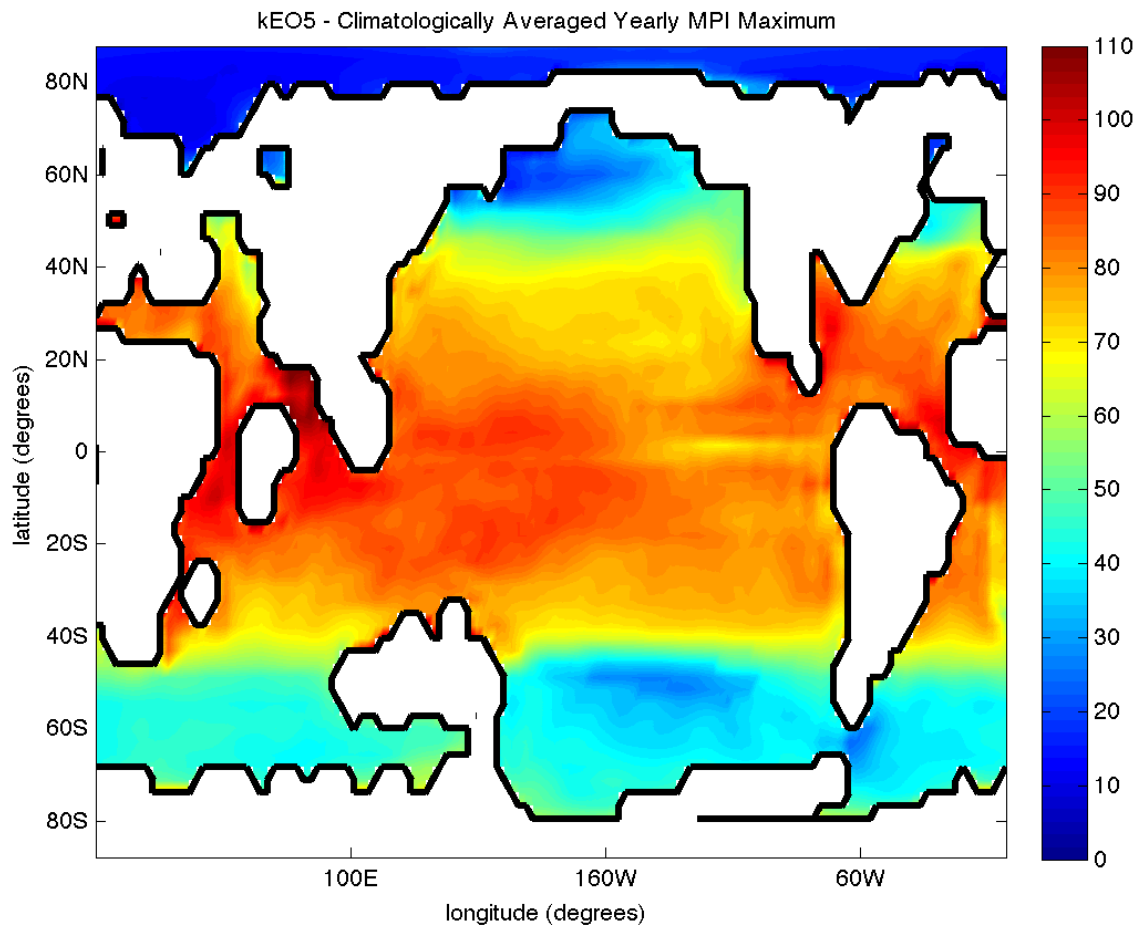


Figure 36: Exceedingly hot climate simulation: Maximum monthly averaged Maximum Potential Intensity (MPI) for the Eocene scheme.